Powder Technology 452 (2025) 120424

Contents lists available at ScienceDirect

Powder Technology

journal homepage: www.journals.elsevier.com/powder-technology

Mass distribution impacts on particle translation and orientation dynamics in dilute flows

Jana Wedel [a,*], Paul Steinmann [a], František Prinz [b], František Lízal [b], Matjaž Hriberšek [c], Jure Ravnik [c]

[a] Friedrich-Alexander-Universitaet Erlangen-Nuernberg, Egerlandstraße 5, Erlangen, 91058, Germany
[b] Brno University of Technology, Technicka 2896, Brno, 616 69, Czech Republic
[c] University of Maribor, Smetanova ul. 17, Maribor, 2000, Slovenia

GRAPHICAL ABSTRACT

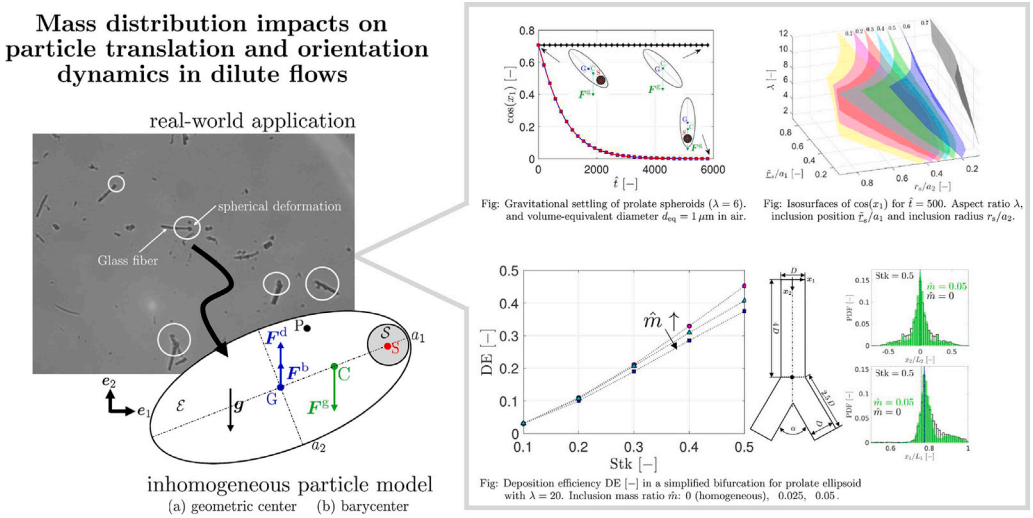

HIGHLIGHTS

- Novel model for translation and orientation dynamics of inhomogeneous ellipsoidal particles.
- The effect of varying the density ratio and aspect ratio on particle dynamics is studied.
- Significant impact on the rotational motion compared to homogeneous ellipsoids.
- Relevant practical applications include particle respiration dynamics.

ARTICLE INFO

Keywords:
Inhomogeneous particles
Spherical inclusion
Lagrangian particle tracking

ABSTRACT

We present a novel model for tracking particles (based on Lagrangian particle tracking) with inhomogeneous mass distribution. Without loss of generality, the presented approach captures inhomogeneity by assuming an offset spherical inclusion in an elongated ellipsoidal particle matrix. The model is first validated on simplified

* Corresponding author.
E-mail address: jana.wedel@fau.de (J. Wedel).

https://doi.org/10.1016/j.powtec.2024.120424
Received 8 July 2024; Received in revised form 30 September 2024; Accepted 2 November 2024
Available online 13 November 2024

Particle deposition

flow configurations such as particles settling in vacuum or air as well as suspended in simple shear and laminar pipe flow, where we achieved an excellent agreement with the available reference results. Furthermore, we investigate the impact of the inclusion parameters on the particle motion. Finally, the deposition of inhomogeneous particles in a simplified bifurcation is analyzed. We conclude that the consideration of inhomogeneity significantly alters the translational and orientational dynamics of the particles. Consequently, we advocate for the consideration of more realistic mass distributions to increase the accuracy of modeling and predicting the motion of inhomogeneous particles in flows for real-world applications.

1. Introduction

Particles in flows are ubiquitous in nature and technology. They range from sludge flocs in wastewater treatment to airborne pollutants such as pollen, dust particles, and fibers to microplastics. In reality, these particles are rarely perfectly shaped or display a perfectly homogeneous mass distribution. Although research in the field of particles suspended in flows spans decades and numerous sophisticated studies can be found in the literature, targeting a wide field of applications ranging from wastewater treatment, [1], to aerosols carrying potential viruses, [2–5], insufficient attention has been paid to the large field of non-spherical and inhomogeneous particles. Despite the fact that naturally occurring particles (blood cells, pollen, dust, fibers) as well as man-made particles (microplastics, asbestos fibers, tire abrasion) are rarely perfect spheres, particles are mostly simplified as spherical in the majority of references, as this greatly reduces the complexity in describing their motion, [6,7]. Authors often resort to shape factors applied to spherical particles that alter the drag force when modeling non-sphericity, [8], but this mostly fails to accurately predict particle motion, [9]. Another commonly used approach to modeling non-spherical particles is to approximate the realistic particle as a prolate spheroid, [1], which is the most studied non-spherical particle shape. In this context, Jeffery, [10], was the first to study single ellipsoids suspended in viscous shear flow and proposed force and torque expressions in uniform shear flow under Stokes conditions. Jeffery, [10], further showed that the motion of the spheroid can be described by periodic orbits and concluded that the initial orientation affects the final state of the particle. Brenner extended the work of Jeffery, [10], to ellipsoids suspended in arbitrary flow conditions, [11, 12]. Like Jeffery [10], Brenner [11,12] also assumes that the inertia of the particles and of the fluid is negligible, [13]. However, for large Reynolds numbers, as shown by Karnis et al. [14,15], inertial effects are important, as the non-spherical particle motion deviates from the results of the Jeffery model. Several authors observed that elongated ellipsoidal particles accumulate in viscous sublayers and tend to gather in areas of low-velocity, [16–18], similar to their spherical counterpart. Furthermore, these spheroids have been found to preferentially align with the mean flow, especially in near-wall regions, [13]. In numerical and experimental studies, Tian et al. [19] investigated the motion of high aspect ratio prolate ellipsoids in laminar pipe flows. Tian et al. [19], found that the particle aspect ratio, the density ratio of particles to fluid and the shear rate of the flow are crucial parameters that significantly change the particle motion. Other authors investigated the alignment of fiber- and disk-shaped particles in near-wall turbulence in a channel flow, see Cui et al. [20]. Cui et al. [20], found the formation of three preferred alignment patterns around ensemble-averaged vortices.

Recently, Ravnik et al. [21], numerically studied asbestos fibers in flows and pointed out the importance of an appropriate shape approximation. They found that it is not sufficient to approximate the asbestos fibers by a simple ellipsoidal shape, as the force and torque values obtained deviate strongly from the real particle shape values. More recently, Wedel et al. [9], performed particle simulations considering superellipsoidal shapes and investigated the effects of non-sphericity in various flow conditions. The authors showed that the use of the presented superellipsoidal models for drag and torque allows the calculation of particle trajectories with superior accuracy compared to simplified non-spherical particle approximations, [9]. Despite the intensive research on non-spherical particle shapes in the field of ellipsoids and superellipsoids, most authors considered homogeneous particles, while the research on inhomogeneous particles is sparse. However, particles are never perfectly homogeneous, such as sludge flocs, dust particles, or even glass fibers produced by mechanical cutting processes. Cui et al. [22], targeted the modeling of sludge-flocs and considered inhomogeneity by assuming a spherical inclusion. However, the authors used a simplified approach, by neglecting the coupling of translational and rotational motion in their approach.

Nonhomogeneous mass distribution is also crucial for various biological organisms such as for example micro-swimmers, which gained significant importance in the scientific field in recent years. The locomotion of various gyrotactic swimmers, including certain plankton species, is influenced by their ability to generate gravitational torque, e.g. from an inhomogeneous mass distribution, [23]. This locomotion tactic is called gyrotaxis, which results from the interplay of gravitational and viscous torques acting on the swimmers when suspended in a flow. Gyrotaxis is among the most widely studied motile response of micro swimmers. For example, Marchioli et al. [23], numerically investigated the dynamics of small spherical and bottom-heavy gyrotactic swimmers dispersed in open-channel flow turbulence using direct-numerical-simulation-based Eulerian–Lagrangian simulations. Moreover, Qui et al. investigated the motion of spherical gyrotactic swimmers suspended in turbulent flows, [24]. The study examined how gyrotaxis affects the orientational dynamics of the swimmers. The findings revealed that the correlation between the time scales of gyrotaxis and turbulence plays a critical role in determining the efficiency of the swimmers' vertical movement through the suspension.

Recently, Rautenbach et al. [25], studied Lagrangian Sensor Particles (LSP) as used in characterizations of stirred tank reactors. In this context, the authors especially examined the effects of mass-center offset, i.e. the shift between center of mass from the geometric center, on the flow-following capabilities of the LSPs. The authors conclude that the internal mass distribution of the LSP has strong impact on its motion and can thus be considered a crucial parameter to optimize the LSP design.

Also in the field of lung studies, where deposition and distribution in realistic human lung replicas are investigated, accurate predictions are crucial as the ability to predict localized concentrations of inhaled toxic fibers can provide decision-makers with critical information to improve measures for human protection, [26]. This awareness of the harmful effects associated with inhaled asbestos originally motivated research into the transport and deposition of fibers within the human airways. More recently, the increased use of carbon nanotubes and other man-made fibers, alongside the potential of using inhaled biodegradable fibers as drug carriers, has revitalized interest in this topic, [27]. Biodegradable fibers could optimize the targeted delivery of medication, offering the ability to penetrate deeper into the lungs than their spherical counterparts and potentially improving the treatment of lower respiratory regions, [28]. The pharmaceutical applications require even higher precision of predictions of local distribution of the inhaled dose and hence the demands for the precision of numerical simulations of the fiber flow are growing. However, up to this day these particles are generally simply assumed to be homogeneous, [26].

As a motivation, we consider real fibers employed in studies of human airway replicas [29] that were prepared by crushing glass

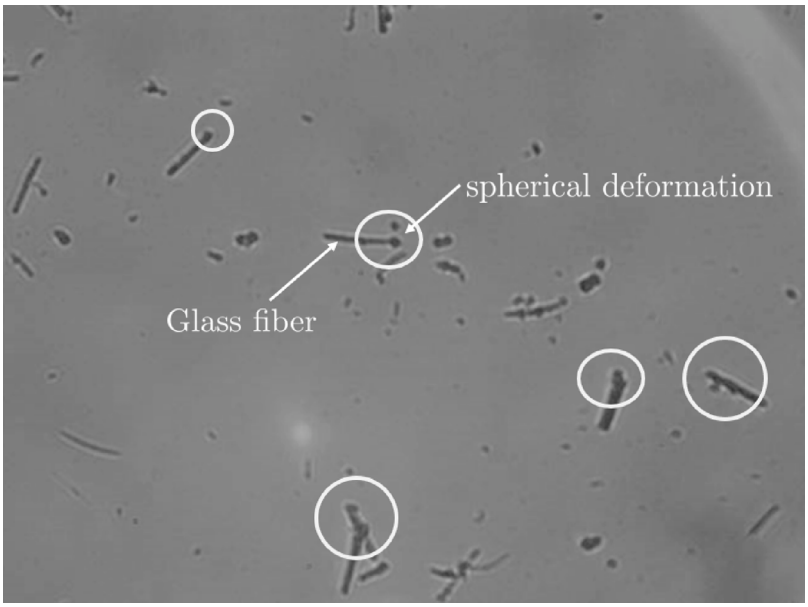

Fig. 1. Glass fibers under microscope employed in lung deposition studies.

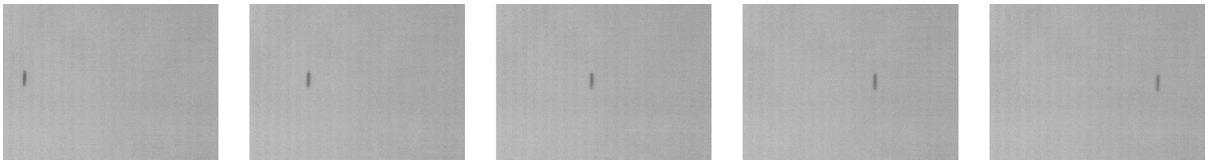

Fig. 2. Glass fiber traveling in laminar pipe flow (Re ≈ 500) with particle long axis oriented perpendicular to the streamwise direction. Frames are presented in $\Delta t = 0.00015$ s intervals.

wool in a mechanical press.[1] This type of glass wool is designed for thermal insulation of attics and other confined spaces. Workers applying this material are at risk of exposure through inhalation if proper personal protection is not used, making the study of these fibers relevant to real-world scenarios. As shown in Fig. 1, although glass fibers are usually considered straight and rigid, they often exhibit attached inhomogeneities that can influence their flow behavior, see Fig. 2, where a glass fiber travels in laminar pipe flow with its particle long axis orientated perpendicular to the streamwise direction. This paper presents a method specifically designed to address the effects of such inhomogeneities on fiber motion.

In order to contribute to a better understanding of the flow of real fibers, this work aims to extend the model proposed by Cui et al. [22], to address the lack of research in the field of particles with inhomogeneous density distribution with a special focus on glass fibers suspended in air. Note that the proposed model takes into account the fully coupled dynamics of inhomogeneous particles, compared to the reference model of Cui et al. [22], which is formulated in the geometric center of the particle, but neglecting the coupling between the translational and rotational dynamics.

2. Lagrange particle tracking of inhomogeneous ellipsoidal particles

2.1. Notation

In this work, we employ bold italic font to express tensors of various orders. Bold italic lowercase letters such as $\boldsymbol{a}$ represent first-order tensors (vectors), while bold italic uppercase letters such as $\boldsymbol{A}$ are used for second-order tensors. We can express the coordinate representation in Cartesian coordinate systems with base vectors $\boldsymbol{e}'_i$, $\boldsymbol{e}_i$ $(i = 1, 2, 3)$ using Einstein's summation convention as

$$\boldsymbol{a} = a'_i\,\boldsymbol{e}'_i = a_i\,\boldsymbol{e}_i \quad \text{and} \quad \boldsymbol{A} = A'_{ij}\,\boldsymbol{e}'_i \otimes \boldsymbol{e}'_j = A_{ij}\,\boldsymbol{e}_i \otimes \boldsymbol{e}_j, \tag{1}$$

where a'_i, a_i and A'_{ij}, A_{ij} are the corresponding coefficients in the coordinate system $\boldsymbol{e}'_i$, $\boldsymbol{e}_i$, respectively. The tensor coefficients a'_i, a_i and A'_{ij}, A_{ij} can be arranged in coefficient matrices, which we denote by underlined italic letters:

$$\underline{a}' = \begin{bmatrix} a'_1 \\ a'_2 \\ a'_3 \end{bmatrix}, \quad \underline{a} = \begin{bmatrix} a_1 \\ a_2 \\ a_3 \end{bmatrix} \quad \text{and} \quad \underline{A}' = \begin{bmatrix} A'_{11} & A'_{12} & A'_{13} \\ A'_{21} & A'_{22} & A'_{23} \\ A'_{31} & A'_{32} & A'_{33} \end{bmatrix},$$
$$\underline{A} = \begin{bmatrix} A_{11} & A_{12} & A_{13} \\ A_{21} & A_{22} & A_{23} \\ A_{31} & A_{32} & A_{33} \end{bmatrix}. \tag{2}$$

Note that the employed notation is consistent with our previous work, [30]. The rotation matrix $\underline{R}$ transforming coefficients with respect to the base vectors $\boldsymbol{e}_i$ to coefficients with respect to the base vectors $\boldsymbol{e}'_i$ is expressed as

$$\underline{R} = \begin{bmatrix} R_{11} & R_{12} & R_{13} \\ R_{21} & R_{22} & R_{23} \\ R_{31} & R_{32} & R_{33} \end{bmatrix} \quad \text{with} \quad R_{ij} = \boldsymbol{e}'_i \cdot \boldsymbol{e}_j \quad \text{and} \quad \boldsymbol{e}'_i = R_{ij}\,\boldsymbol{e}_j. \tag{3}$$

The corresponding rotation tensor $\boldsymbol{R} = \boldsymbol{e}'_j \otimes \boldsymbol{e}_j$ mapping $\boldsymbol{e}_j$ into $\boldsymbol{e}'_j = \boldsymbol{R} \cdot \boldsymbol{e}_j$ has therefore coordinate representation $\boldsymbol{R} = [\boldsymbol{e}'_j \cdot \boldsymbol{e}_i]\,\boldsymbol{e}_i \otimes \boldsymbol{e}_j = R_{ji}\,\boldsymbol{e}_i \otimes \boldsymbol{e}_j$, i.e. the coefficient matrix of $\boldsymbol{R}$ is the matrix transpose $\underline{R}^t$ of the rotation matrix $\underline{R}$. Taken together, coefficient matrices of vectors and second order tensors transform as

$$\underline{a}' = \underline{R}\,\underline{a} \quad \text{and} \quad \underline{A}' = \underline{R}\,\underline{A}\,\underline{R}^t. \tag{4}$$

[1] The fibers were prepared by crushing Supafil® Loft glass wool (Knauf Insulation GmbH, Simbach am Inn, Germany). The fiber diameter was 3.8 ±1.4 μm and length 37.1 ±20.9 μm, see Fig. 1.

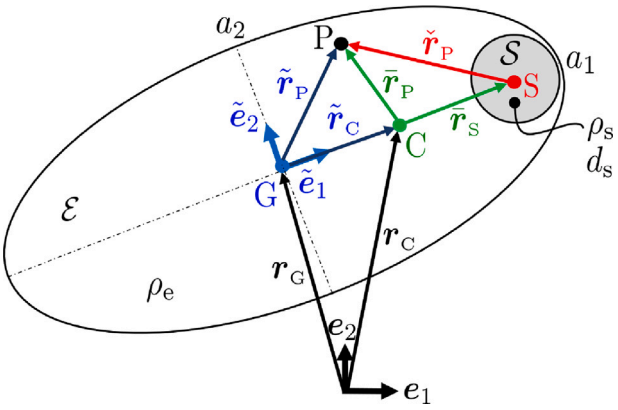

Fig. 3. Sketch of an inhomogeneous prolate ellipsoid with a spherical mass inclusion. Here, G denotes the body fixed center of geometry, C the barycenter, S the center of the spherical inclusion, and P an arbitrary point. The density of the inclusion is denoted by ρ_s, while the enclosing ellipsoid matrix has a density of ρ_e. The particle long axis is a_1, while the particle minor axes are a_2 and a_3, respectively. For a prolate spheroidal particle $a_2 = a_3$. Here $\mathcal{E}$ and $\mathcal{S}$ denote the integration domains for the entire ellipsoid and the spherical inclusion. Note that the particle frame of reference (pFoR) is indicated by $\tilde{\boldsymbol{e}}_i$, $i = 1, 2, 3$.

2.2. Kinematics of a rigid body

We present a novel approach for the modeling of realistic particles of non-spherical shape and with inhomogeneous mass distribution, as observed commonly in real-world applications (glass or asbestos fibers, [21], sludge flocs, [1]), to compute their translational and orientational dynamics. This approach serves as an extension of the model presented by Cui et al. [1], in which the inhomogeneity in prolate spheroids is modeled by spherical regional inclusions of different densities. Cui et al. target sludge flocs and therefore use a simplification in which the translational and orientational motion are treated as decoupled. As will be shown later, this simplification holds for the sludge flocs considered. However, for fibers in air, the assumption is not justified. In agreement with Cui et al. [1], we focus on spherical inclusions with density ρ_s and diameter $d_s = 2r_s$, see Fig. 3. Note that the presented approach is easily extendable to arbitrarily shaped inclusions. As displayed in Fig. 3, we denote the body fixed particle geometric center as G, the barycenter as C, the center of the spherical inclusion S and an arbitrary point as P. Note that by introducing an inhomogeneity located at $\boldsymbol{r}_S$, the barycenter C no longer coincides with the particle geometric center G, see Fig. 3.

In the following, we will denote position vectors from the origin of the inertial frame of reference (iFoR) using bold $\boldsymbol{r}$ with the terminating point as a **sub**script. Furthermore, position vectors with origin in either G, C or S are indicated by $[\tilde{\cdot}]$, $[\bar{\cdot}]$ or $[\check{\cdot}]$, respectively. In the geometric center G we may append the particle frame of reference (pFoR) with orthonormal triad $\tilde{\boldsymbol{e}}_i$ $(i = 1, 2, 3)$ moving with the particle to later express vectors and tensors in coordinate representation. Recall the Euler representation for the kinematics of an arbitrary point P on the rigid body

$$\boldsymbol{r}_P = \boldsymbol{r}_C + \bar{\boldsymbol{r}}_P, \boldsymbol{v}_P = \boldsymbol{v}_C + \bar{\boldsymbol{v}}_P, \boldsymbol{a}_P = \boldsymbol{a}_C + \bar{\boldsymbol{a}}_P, \tag{5}$$

with

$$\bar{\boldsymbol{v}}_P = \bar{\boldsymbol{r}}'_{P\times} \cdot \boldsymbol{\omega} = \boldsymbol{\omega}_\times \cdot \bar{\boldsymbol{r}}_{P\times}, \bar{\boldsymbol{a}}_P = \bar{\boldsymbol{r}}'_{P\times} \cdot \dot{\boldsymbol{\omega}} + \boldsymbol{\omega}_\times^2 \cdot \bar{\boldsymbol{r}}_{P\times}. \tag{6}$$

In Eqs. ((5),(6)), the barycenter velocity of the particle is denoted by $\boldsymbol{v}_C$ and the particle's angular velocity by $\boldsymbol{\omega}$, while $\boldsymbol{a}_C$ and $\dot{\boldsymbol{\omega}}$ denote the barycenter translational and angular acceleration of the particle, respectively. Herein we use the notation for the skewsymmetric spin tensor, indicated by $[\cdot]_\times$, of an axial vector, to express the vector product of two vectors in various alternative but equivalent ways:

$$\boldsymbol{a} \times \boldsymbol{b} = \boldsymbol{b}'_\times \cdot \boldsymbol{a} = \boldsymbol{a}_\times \cdot \boldsymbol{b}. \tag{7}$$

The coordinate representation of a skew symmetric spin tensor $\underline{a}_\times$ reads as

$$\underline{a}_\times = \begin{bmatrix} 0 & -a_3 & a_2 \\ a_3 & 0 & -a_1 \\ -a_2 & a_1 & 0 \end{bmatrix}. \tag{8}$$

By specializing P to G and by reordering terms and using the alternative notation for the vector product, the acceleration of the barycenter C is eventually expressed in terms of the acceleration of the center of geometry G, the angular velocity and angular acceleration and the position vector pointing from G to C, as an intermediate result, as

$$\boldsymbol{a}_C = \boldsymbol{a}_G + \tilde{\boldsymbol{r}}'_{C\times} \cdot \dot{\boldsymbol{\omega}} + \boldsymbol{\omega} \times \left[\tilde{\boldsymbol{r}}'_{C\times} \cdot \boldsymbol{\omega}\right]. \tag{9}$$

Remark 2.1. In this work, we described the orientation of a particle in space by quaternions $\underline{q} = [q_0, q_1, q_2, q_3]'$. The quaternions (Euler parameters) can be determined from the Euler angles $(\varphi_i,\ i = 1, 2, 3)$ using

$$\underline{q} = \begin{bmatrix} q_0 \\ q_1 \\ q_2 \\ q_3 \end{bmatrix} = \begin{bmatrix} \cos\left[0.5\left[\varphi_1 + \varphi_3\right]\right] \cos\left[\varphi_2/2\right] \\ \cos\left[0.5\left[\varphi_1 - \varphi_3\right]\right] \sin\left[\varphi_2/2\right] \\ \sin\left[0.5\left[\varphi_1 - \varphi_3\right]\right] \sin\left[\varphi_2/2\right] \\ \sin\left[0.5\left[\varphi_1 + \varphi_3\right]\right] \cos\left[\varphi_2/2\right] \end{bmatrix} \tag{10}$$

and are subject to the constraint $q_0^2 + q_1^2 + q_2^2 + q_3^2 = 1$, [31]. The rotation matrix in the inertia frame then follows as

$$\underline{R} = \begin{bmatrix} q_0^2 + q_1^2 - q_2^2 - q_3^2 & 2[q_1 q_2 + q_0 q_3] & 2[q_1 q_3 - q_0 q_2] \\ 2[q_1 q_2 - q_0 q_3] & q_0^2 - q_1^2 + q_2^2 - q_3^2 & 2[q_2 q_3 - q_0 q_1] \\ 2[q_1 q_3 + q_0 q_2] & 2[q_2 q_3 - q_0 q_1] & q_0^2 - q_1^2 - q_2^2 + q_3^2 \end{bmatrix}. \tag{11}$$

In addition, the evolution of the quaternions is related to the angular particle velocity in the particle frame $\underline{\omega}'$ as

$$d\underline{q}/dt = \begin{bmatrix} dq_0/dt \\ dq_1/dt \\ dq_2/dt \\ dq_3/dt \end{bmatrix} = \frac{1}{2} \begin{bmatrix} -q_1 & -q_2 & -q_3 \\ q_0 & -q_3 & q_2 \\ q_3 & q_0 & -q_1 \\ -q_2 & q_1 & q_0 \end{bmatrix} \underline{\omega}'. \tag{12}$$

Remark 2.2. The Stokes number Stk describes the ratio of the characteristic particle response time τ_p to a characteristic time of the flow τ_f and can be obtained using the volume-equivalent sphere diameter d_{eq}, a characteristic length L_0 and a characteristic flow velocity u_0 as

$$\mathrm{Stk} = \frac{\tau_p}{\tau_f} = \frac{\rho_p}{\rho_f} \frac{d_{eq}^2 u_0}{18 \nu_f L_0} \quad \text{with} \quad \tau_p = \frac{\rho_p}{\rho_f} \frac{d_{eq}^2}{18 \nu_f} \quad \text{and} \quad \tau_f = \frac{L_0}{u_0}. \tag{13}$$

Here, ρ_p denotes the average particle density ($\rho_p = m/V$, where m denotes the resulting particle mass and V the particle volume), while ρ_f and ν_f denote the fluid density and kinematic viscosity, respectively. The terminal velocity $\boldsymbol{v}_t$ of a spherical particle settling in Stokes flow is given by [32]

$$\boldsymbol{v}_t = \frac{d_{eq}^2}{18 \nu_f} \frac{\rho_p - \rho_f}{\rho_f} \boldsymbol{g}. \tag{14}$$

The particle Reynolds number Re_p is defined as follows:

$$\mathrm{Re}_p = \frac{d_{eq} |\boldsymbol{u}_{rel}|}{\nu_f}, \tag{15}$$

where $\boldsymbol{u}_{rel} = \boldsymbol{u} - \boldsymbol{v}_C$ denotes the relative velocity between the particle barycenter $\boldsymbol{v}_C$ and the fluid $\boldsymbol{u}$.

In the experimental work of Di Giusto et al. [33], the authors investigated the rotational dynamics of neutrally buoyant spheroidal

and cylindrical particles suspended in simple shearing flows in the small-inertia regime ($\mathrm{Re_p} = \mathrm{Stk} \lesssim 1$). The authors found that for these weakly inertial ellipsoids, while exhibiting no significant effect on the period of rotation, a systematic drift away from the Jeffery orbits and towards limiting stable orbits is reported, necessitating suitable corrections. Note that in the following, we will only consider cases where the particle Reynolds number is mostly $\mathrm{Re_p} \ll 1$. $\mathrm{Re_p} \approx 1$ are observed only instantaneously at the injection time if the relative particle is released with zero initial velocity as here the relative velocity $|\boldsymbol{u}_{\mathrm{rel}}|$ is maximal. Thus, we expect no drift from the Jeffery orbits due to inertia effects throughout the conducted simulations.

2.3. Inertia of a rigid body

To start with, we define the density distribution as

$$\begin{aligned} \rho &= \rho_{\mathrm{e}} && \text{in} \quad \mathcal{E}\backslash\mathcal{S}, \\ \rho &= \rho_{\mathrm{e}} + \Delta\rho_{\mathrm{s}} && \text{in} \quad \mathcal{S}. \end{aligned} \tag{16}$$

wherein we use $\Delta\rho_{\mathrm{s}}$ to indicate the difference of the density in the spherical inclusion $\mathcal{S}$ and the ellipsoid $\mathcal{E}$. Here $\mathcal{E}$ and $\mathcal{S}$ denote the integration domains for the entire ellipsoid and the spherical inclusion. Then the resulting mass for the particle, the homogeneous (reference) ellipsoid and the mass difference between the spherical inclusion and the inhomogeneous ellipsoid read

$$m = \int_{\mathcal{E}} \rho \mathrm{d}v = m_{\mathrm{e}} + \Delta m_{\mathrm{s}} = \int_{\mathcal{E}} \rho_{\mathrm{e}} \mathrm{d}v + \int_{\mathcal{S}} \Delta\rho_{\mathrm{s}} \mathrm{d}v \tag{17}$$

The tensor of inertia of a rigid body with respect to its barycenter reads

$$\boldsymbol{J}_{\mathrm{C}} = \int_{\mathcal{E}} \rho \tilde{\boldsymbol{r}}^{t}_{\mathrm{P}\times} \cdot \tilde{\boldsymbol{r}}_{\mathrm{P}\times} \mathrm{d}v. \tag{18}$$

This expression follows directly from the expression of the rotational part of the kinetic energy of a rigid body and our above notation for the vector product

$$\int_{\mathcal{E}} \rho |\bar{\boldsymbol{v}}_{\mathrm{P}}|^2 \mathrm{d}v = \boldsymbol{\omega} \cdot \int_{\mathcal{E}} \rho \tilde{\boldsymbol{r}}^{t}_{\mathrm{P},\times} \cdot \tilde{\boldsymbol{r}}_{\mathrm{P}\times} \mathrm{d}v \cdot \boldsymbol{\omega} \tag{19}$$

Then the Steiner theorem renders for the tensor of inertia with respect to the center of geometry (please note the positive sign since we use the transpose on one of the skewsymmetric spin tensors)

$$\boldsymbol{J}_{\mathrm{G}} = \boldsymbol{J}_{\mathrm{C}} + m\tilde{\boldsymbol{r}}^{t}_{\mathrm{C}\times} \cdot \tilde{\boldsymbol{r}}_{\mathrm{C}\times}. \tag{20}$$

Observe that from a practical standpoint it is easiest to directly compute the tensor of inertia with respect to the center of geometry from

$$\boldsymbol{J}_{\mathrm{G}} = \boldsymbol{J}_{\mathrm{e}} + \Delta\boldsymbol{J}_{\mathrm{s}} + \Delta m_s \tilde{\boldsymbol{r}}^{t}_{\mathrm{S}\times} \cdot \tilde{\boldsymbol{r}}_{\mathrm{S}\times} \tag{21}$$

with tensor of inertia of the homogeneous (reference) ellipsoid with respect to the center of geometry $\boldsymbol{J}_{\mathrm{e}}$ as

$$\boldsymbol{J}_{\mathrm{e}} = \int_{\mathcal{E}} \rho_{\mathrm{e}} \tilde{\boldsymbol{r}}^{t}_{\mathrm{P}\times} \cdot \tilde{\boldsymbol{r}}_{\mathrm{P}\times} \mathrm{d}v \tag{22}$$

and the difference tensor of inertia of the spherical inclusion with respect to its own barycenter $\boldsymbol{J}_{\mathrm{s}}$ as

$$\Delta\boldsymbol{J}_{\mathrm{s}} = \int_{\mathcal{S}} \Delta\rho_s \check{\boldsymbol{r}}^{t}_{\mathrm{P}\times} \cdot \check{\boldsymbol{r}}_{\mathrm{P}\times} \mathrm{d}v. \tag{23}$$

From this, the tensor of inertia with respect to the barycenter J_{C} of the rigid body may be retrieved by combining Eqs. ((20),(21)).

Remark 2.3. The moment of inertia matrix of the homogeneous ellipsoidal particle in the pFoR can be obtained as [34]

$$\underline{J}'_{\mathrm{e}} = \frac{1}{5} m_{\mathrm{e}} \begin{bmatrix} 2a_3^2 & 0 & 0 \\ 0 & a_3^2\left[1+\lambda^2\right] & 0 \\ 0 & 0 & a_3^2\left[1+\lambda^2\right] \end{bmatrix}, \tag{24}$$

where for prolate spheroids the aspect ratio renders $\lambda = a_1/a_3$ with the semi-major axis denoted as a_1 and the semi-minor axis as $a_2 = a_3$. The moment of inertia tensor of the spherical inclusion difference in the pFoR renders

$$\Delta\underline{J}'_{\mathrm{s}} = \frac{2}{3}\Delta m_{\mathrm{s}} \begin{bmatrix} r_{\mathrm{s}}^2 & 0 & 0 \\ 0 & r_{\mathrm{s}}^2 & 0 \\ 0 & 0 & r_{\mathrm{s}}^2 \end{bmatrix}, \tag{25}$$

with the inclusion radius r_{s}.

2.4. Kinetics of a rigid body

In the following, we will express the kinetics of a rigid body, both with respect to (a) the barycentric and (b) the geometric center. Observe that both formulations are valid and their equivalence will be demonstrated in the following. However, each formulation requires careful consideration of the respective translational and rotational dynamics.

(a) with respect to the barycenter C

The translational and rotational balance of momentum read with respect to the barycenter C as

$$\boldsymbol{F} = m\boldsymbol{a}_{\mathrm{C}}, \tag{26}$$

$$\boldsymbol{T}_{\mathrm{C}} = \boldsymbol{J}_{\mathrm{C}} \cdot \dot{\boldsymbol{\omega}} + \boldsymbol{\omega} \times \left[\boldsymbol{J}_{\mathrm{C}} \cdot \boldsymbol{\omega}\right]. \tag{27}$$

For a unified representation they may be compacted into a (uncoupled) system as

$$\begin{bmatrix} \boldsymbol{F} \\ \boldsymbol{T}_{\mathrm{C}} \end{bmatrix} = \begin{bmatrix} m\boldsymbol{I} & \boldsymbol{0} \\ \boldsymbol{0} & \boldsymbol{J}_{\mathrm{C}} \end{bmatrix} \cdot \begin{bmatrix} \boldsymbol{a}_{\mathrm{C}} \\ \dot{\boldsymbol{\omega}} \end{bmatrix} + \begin{bmatrix} \boldsymbol{0} \\ \boldsymbol{\omega} \times \left[\boldsymbol{J}_{\mathrm{C}} \cdot \boldsymbol{\omega}\right] \end{bmatrix}. \tag{28}$$

Here, $\boldsymbol{T}_{\mathrm{C}}$ denotes the resulting torque exerted on the particle with respect to its barycenter and $\boldsymbol{F}$ is the resulting force exerted on the particle.

(b) with respect to the geometric center G

With respect to the center of geometry G the translational and rotational balance of momentum read[2]

$$\boldsymbol{F} = m\boldsymbol{a}_{\mathrm{G}} + m\tilde{\boldsymbol{r}}^{t}_{\mathrm{C}\times} \cdot \dot{\boldsymbol{\omega}} + \boldsymbol{\omega} \times \left[m\tilde{\boldsymbol{r}}^{t}_{\mathrm{C}\times} \cdot \boldsymbol{\omega}\right], \tag{29}$$

$$\boldsymbol{T}_{\mathrm{G}} = m\tilde{\boldsymbol{r}}_{\mathrm{C}\times} \cdot \boldsymbol{a}_{\mathrm{G}} + \boldsymbol{J}_{\mathrm{G}} \cdot \dot{\boldsymbol{\omega}} + \boldsymbol{\omega} \times \left[\boldsymbol{J}_{\mathrm{G}} \cdot \boldsymbol{\omega}\right]. \tag{30}$$

For a unified representation they may be compacted into a (coupled) system as

$$\begin{bmatrix} \boldsymbol{F} \\ \boldsymbol{T}_{\mathrm{G}} \end{bmatrix} = \begin{bmatrix} m\boldsymbol{I} & m\tilde{\boldsymbol{r}}^{t}_{\mathrm{C}\times} \\ m\tilde{\boldsymbol{r}}_{\mathrm{C}\times} & \boldsymbol{J}_{\mathrm{G}} \end{bmatrix} \cdot \begin{bmatrix} \boldsymbol{a}_{\mathrm{G}} \\ \dot{\boldsymbol{\omega}} \end{bmatrix} + \begin{bmatrix} \boldsymbol{\omega} \times \left[m\tilde{\boldsymbol{r}}^{t}_{\mathrm{C}\times} \cdot \boldsymbol{\omega}\right] \\ \boldsymbol{\omega} \times \left[\boldsymbol{J}_{\mathrm{G}} \cdot \boldsymbol{\omega}\right] \end{bmatrix}, \tag{31}$$

Here, $\boldsymbol{T}_{\mathrm{G}}$ denotes the resulting torque exerted on the particle with respect to its geometric center.

2.5. Force and torque exerted on a rigid body

In the following, we will discuss (a) the resultant force $\boldsymbol{F}$ as well as (b) the resultant torque $\boldsymbol{T}$ with respect to the barycenter and the geometric center. Observe, that careful consideration of the acting forces and torques is required for the respective formulation. The individual forces contributing to $\boldsymbol{F}$ and their point of application in the inhomogeneous particle are displayed in Fig. 4.

(a) Resultant Force $\boldsymbol{F}$

[2] The former follows directly from inserting the previous intermediate result $\boldsymbol{a}_{\mathrm{C}} = \boldsymbol{a}_{\mathrm{G}} + \tilde{\boldsymbol{r}}^{t}_{\mathrm{C}\times}\dot{\boldsymbol{\omega}} + \boldsymbol{\omega} \times \left[\tilde{\boldsymbol{r}}^{t}_{\mathrm{C}\times} \cdot \boldsymbol{\omega}\right]$. The latter follows from the external torque expressed with respect to the center of geometry $\boldsymbol{T}_{\mathrm{G}} = \boldsymbol{T}_{\mathrm{C}} + \tilde{\boldsymbol{r}}_{\mathrm{C}} \times \boldsymbol{F}$ using the above expression for $\boldsymbol{F}$, recalling the relation $\boldsymbol{J}_{\mathrm{G}} = \boldsymbol{J}_{\mathrm{C}} + m\tilde{\boldsymbol{r}}^{t}_{\mathrm{C}\times} \cdot \tilde{\boldsymbol{r}}_{\mathrm{C}\times}$ and using the identity $\tilde{\boldsymbol{r}}_{\mathrm{C}\times} \cdot \left[\boldsymbol{\omega} \times \left[\tilde{\boldsymbol{r}}^{t}_{\mathrm{C}\times} \cdot \boldsymbol{\omega}\right]\right] = \tilde{\boldsymbol{r}}_{\mathrm{C}} \times \left[\boldsymbol{\omega} \times \left[\boldsymbol{\omega} \times \tilde{\boldsymbol{r}}_{\mathrm{C}}\right]\right] = \boldsymbol{\omega} \times \left[\tilde{\boldsymbol{r}}_{\mathrm{C}} \times \left[\boldsymbol{\omega} \times \tilde{\boldsymbol{r}}_{\mathrm{C}}\right]\right] = \boldsymbol{\omega} \times \left[\tilde{\boldsymbol{r}}^{t}_{\mathrm{C}\times} \cdot \tilde{\boldsymbol{r}}_{\mathrm{C}\times} \cdot \boldsymbol{\omega}\right]$.

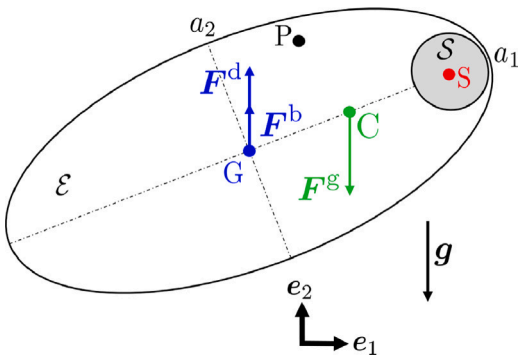

Fig. 4. Sketch of the forces contributing to the resultant $\boldsymbol{F}$ acting on an inhomogeneous prolate ellipsoid with a spherical mass inclusion. Here, $\boldsymbol{F}^{\mathrm{g}}$ denotes the gravity force, $\boldsymbol{F}^{\mathrm{b}}$ denotes the buoyancy force and $\boldsymbol{F}^{\mathrm{d}}$ denotes the drag force. As indicated, $\boldsymbol{F}^{\mathrm{b}}$ and $\boldsymbol{F}^{\mathrm{d}}$ act on the geometrical center G, while $\boldsymbol{F}^{\mathrm{g}}$ acts on the barycenter C. Note that in this sketch the gravitational direction is pointing in the direction of $-\boldsymbol{e}_2$.

The resultant force acting on a rigid body is **independent** from the reference point.[3] As shown in Wedel et al. [30], for a micron-sized ellipsoidal rigid body immersed in Stokes flow with $\rho_{\mathrm{p}} \gg \rho_{\mathrm{f}}$ the dominant force contributions are drag $\boldsymbol{F}^{\mathrm{d}}$, gravity $\boldsymbol{F}^{\mathrm{g}}$ and buoyancy $\boldsymbol{F}^{\mathrm{b}}$, while additional force contributions such as pressure gradient and added mass can be considered negligible, which is especially true for particles suspended in air. It was further shown that even if $\rho_{\mathrm{f}} \approx \rho_{\mathrm{p}}$, the two latter force contributions are way smaller than drag, buoyancy and gravity contribution if the Stokes number is $\mathrm{Stk} \ll 1$ and thus still negligible. It is important to note that the gravity contribution acts on the barycenter C, while the drag and buoyancy contribution act on the geometrical center G. To summarize, the resultant force for the considered applications is obtained as

$$\boldsymbol{F} = \boldsymbol{F}^{\mathrm{g}} + \boldsymbol{F}^{\mathrm{b}} + \boldsymbol{F}^{\mathrm{d}}. \tag{32}$$

These expand as

$$\boldsymbol{F}^{\mathrm{g}} = + \int_{\mathcal{E}} \rho \boldsymbol{g} \mathrm{d}v = \quad m\boldsymbol{g} \tag{33}$$

$$\boldsymbol{F}^{\mathrm{b}} = - \int_{\mathcal{E}} \rho_{\mathrm{f}} \boldsymbol{g} \mathrm{d}v = -m_{\mathrm{f}} \boldsymbol{g} \tag{34}$$

$$\boldsymbol{F}^{\mathrm{d}} = \int_{\partial\mathcal{E}} \boldsymbol{t} \mathrm{d}a = \int_{\partial\mathcal{E}} \left[\bar{\boldsymbol{t}} + \tilde{\boldsymbol{t}}\right] \mathrm{d}a = \int_{\partial\mathcal{E}} \bar{\boldsymbol{t}} \mathrm{d}a = \pi \mu_{\mathrm{f}} a_3 \boldsymbol{K} \cdot \left[\boldsymbol{u} - \boldsymbol{v}_{\mathrm{G}}\right]. \tag{35}$$

The expression of the drag resistance tensor $\boldsymbol{K}$ in the pFoR can be found in the Appendix. Note that the traction $\boldsymbol{t}$ can be decomposed into a surface average $\bar{\boldsymbol{t}}$, i.e. a constant vector, and a fluctuation contribution $\tilde{\boldsymbol{t}}$ as

$$\boldsymbol{t} = \bar{\boldsymbol{t}} + \tilde{\boldsymbol{t}} \quad \text{with} \quad \bar{\boldsymbol{t}} := \frac{1}{\mathrm{sur}(\partial\mathcal{E})} \int_{\partial\mathcal{E}} \boldsymbol{t} \, \mathrm{d}a \quad \text{and} \quad \boldsymbol{0} \equiv \int_{\partial\mathcal{E}} \tilde{\boldsymbol{t}} \, \mathrm{d}a. \tag{36}$$

Thus, in Eq. (35) the resultant of the traction variation vanishes, i.e. $\int_{\partial\mathcal{E}} \tilde{\boldsymbol{t}} \mathrm{d}a = \boldsymbol{0}$, and consequently only $\bar{\boldsymbol{t}}$ contributes to the drag force. Observe also the velocity of the **center of geometry** $\boldsymbol{v}_{\mathrm{G}}$ of the particle in the drag expression. This may be re-expressed in terms of the barycenter velocity by

$$\boldsymbol{v}_{\mathrm{C}} = \boldsymbol{v}_{\mathrm{G}} + \tilde{\boldsymbol{r}}^{t}_{\mathrm{c}\times} \cdot \boldsymbol{\omega}. \tag{37}$$

(b) Resultant Torque

The resultant torque acting on a rigid body generally **depends** on the reference point. In the following, we will express the torque (b1) in the barycenter as well as (b2) in the geometric center. Furthermore, the Jeffery torque is discussed in (b3).

(b1) with respect to the barycenter C

The resultant torque $\boldsymbol{T}_{\mathrm{C}}$ with respect to the barycenter C consists of a gravity $\boldsymbol{T}^{\mathrm{g}}_{\mathrm{C}}$, a buoyancy $\boldsymbol{T}^{\mathrm{b}}_{\mathrm{C}}$, a drag $\boldsymbol{T}^{\mathrm{d}}_{\mathrm{C}}$ and a Jeffery contribution $\boldsymbol{T}^{\mathrm{j}}$ and reads as

$$\boldsymbol{T}_{\mathrm{C}} = \boldsymbol{T}^{\mathrm{g}}_{\mathrm{C}} + \boldsymbol{T}^{\mathrm{b}}_{\mathrm{C}} + \boldsymbol{T}^{\mathrm{d}}_{\mathrm{C}} + \boldsymbol{T}^{\mathrm{j}} \tag{38}$$

with the gravity, buoyancy, and drag contribution

$$\boldsymbol{T}^{\mathrm{g}}_{\mathrm{C}} = + \int_{\mathcal{E}} \rho \bar{\boldsymbol{r}}_{\mathrm{P}} \times \boldsymbol{g} \mathrm{d}v \; = \boldsymbol{0}, \tag{39}$$

$$\boldsymbol{T}^{\mathrm{b}}_{\mathrm{C}} = - \int_{\mathcal{E}} \rho_{\mathrm{f}} \bar{\boldsymbol{r}}_{\mathrm{P}} \times \boldsymbol{g} \mathrm{d}v = \bar{\boldsymbol{r}}_{\mathrm{G}} \times \boldsymbol{F}^{\mathrm{b}}, \tag{40}$$

$$\boldsymbol{T}^{\mathrm{d}}_{\mathrm{C}} = + \int_{\partial\mathcal{E}} \bar{\boldsymbol{r}}_{\mathrm{P}} \times \bar{\boldsymbol{t}} \mathrm{d}a \; = \bar{\boldsymbol{r}}_{\mathrm{G}} \times \boldsymbol{F}^{\mathrm{d}}. \tag{41}$$

(b2) with respect to the geometric center G

For a micron-sized ellipsoidal rigid body immersed in Stokes flow the resultant torque $\boldsymbol{T}_{\mathrm{G}}$ with respect to the center of geometry G consists of a gravity $\boldsymbol{T}^{\mathrm{g}}_{\mathrm{G}}$, a buoyancy $\boldsymbol{T}^{\mathrm{b}}_{\mathrm{G}}$, a drag $\boldsymbol{T}^{\mathrm{d}}_{\mathrm{G}}$ and a Jeffery contribution $\boldsymbol{T}^{\mathrm{j}}$ and reads as

$$\boldsymbol{T}_{\mathrm{G}} = \boldsymbol{T}^{\mathrm{g}}_{\mathrm{G}} + \boldsymbol{T}^{\mathrm{b}}_{\mathrm{G}} + \boldsymbol{T}^{\mathrm{d}}_{\mathrm{G}} + \boldsymbol{T}^{\mathrm{j}} \tag{42}$$

with the gravity, buoyancy, and drag contribution

$$\boldsymbol{T}^{\mathrm{g}}_{\mathrm{G}} = + \int_{\mathcal{E}} \rho \tilde{\boldsymbol{r}}_{\mathrm{P}} \times \boldsymbol{g} \mathrm{d}v \; = \tilde{\boldsymbol{r}}_{\mathrm{c}} \times \boldsymbol{F}^{\mathrm{g}}, \tag{43}$$

$$\boldsymbol{T}^{\mathrm{b}}_{\mathrm{G}} = - \int_{\mathcal{E}} \rho_{\mathrm{f}} \tilde{\boldsymbol{r}}_{\mathrm{P}} \times \boldsymbol{g} \mathrm{d}v \; = \boldsymbol{0}, \tag{44}$$

$$\boldsymbol{T}^{\mathrm{d}}_{\mathrm{G}} = + \int_{\partial\mathcal{E}} \tilde{\boldsymbol{r}}_{\mathrm{P}} \times \bar{\boldsymbol{t}} \mathrm{d}a \; = \boldsymbol{0}. \tag{45}$$

Observe that the sum of the gravity, buoyancy, and drag contributions in (b1) and (b2) due to $\tilde{\boldsymbol{r}}_{\mathrm{C}} = -\bar{\boldsymbol{r}}_{\mathrm{C}}$ satisfies the condition $\boldsymbol{T}_{\mathrm{G}} = \boldsymbol{T}_{\mathrm{C}} + \tilde{\boldsymbol{r}}_{\mathrm{C}} \times \boldsymbol{F}$.

(b3) Jeffery torque

Finally, the Jefferey contribution to the torque is a free couple and thus **independent** of the reference point. It results as

$$\boldsymbol{T}^{\mathrm{j}} = \int_{\partial\mathcal{E}} \tilde{\boldsymbol{r}}_{\mathrm{P}} \times \tilde{\boldsymbol{t}} \, \mathrm{d}a = \int_{\partial\mathcal{E}} \bar{\boldsymbol{r}}_{\mathrm{P}} \times \tilde{\boldsymbol{t}} \, \mathrm{d}a = 2 \, \tilde{\boldsymbol{\sigma}}^{\mathrm{skw}}_{a} \, \mathrm{vol}(\mathcal{E}), \tag{46}$$

where the Jefferey traction (fluctuation) as the integral over the traction fluctuations over the boundary is $\int_{\partial\mathcal{E}} \tilde{\boldsymbol{t}} \, da = \boldsymbol{0}$. Note that the **super**script skw indicates the skew-symmetry of the specific tensor, while the **sub**script a denotes the axialvector. Thus, the Jeffery torque is invariant to the reference frame, i.e. $\boldsymbol{T}^{\mathrm{j}}_{\mathrm{G}} = \boldsymbol{T}^{\mathrm{j}}_{\mathrm{C}}$[4], since the Jeffery traction satisfies $\int_{\partial\mathcal{E}} \tilde{\boldsymbol{t}} \, \mathrm{d}a = \boldsymbol{0}$ and expands in terms of a spatially constant Cauchy-type stress as $\tilde{\boldsymbol{t}} = \tilde{\boldsymbol{\sigma}} \cdot \boldsymbol{n}$.

Remark 2.4. In the particle frame of reference the Jeffery torque can be obtained using

$$\underline{T}^{\mathrm{j}} = \pi \mu_{\mathrm{f}} c^3 \left[\underline{\Pi}' \cdot \begin{bmatrix} d'_{\mathrm{f}\,32} \\ d'_{\mathrm{f}\,13} \\ d'_{\mathrm{f}\,12} \end{bmatrix} + \underline{\Omega}' \cdot \begin{bmatrix} w'_{\mathrm{f}\,32} - \omega'_1 \\ w'_{\mathrm{f}\,13} - \omega'_2 \\ w'_{\mathrm{f}\,21} - \omega'_3 \end{bmatrix} \right], \tag{47}$$

where $\underline{\Omega}'$ is the rotation resistance coefficient matrix and $\underline{\Pi}'$ the deformation resistance coefficient matrix in the pFoR. In addition, $d'_{\mathrm{f}\,ij}$ and $w'_{\mathrm{f}\,ij}$ with $i, j = 1, 2, 3$ denote the coefficients of the deformation rate tensor and spin tensor in the particle frame of reference. Note that the deformation rate and spin tensor are obtained using $\boldsymbol{d}_{\mathrm{f}} = 0.5 \left[\nabla \boldsymbol{u} + \nabla \boldsymbol{u}^{t}\right]$ and $\boldsymbol{w}_{\mathrm{f}} = 0.5 \left[\nabla \boldsymbol{u} - \nabla \boldsymbol{u}^{t}\right]$, respectively. The expression for the resistance tensor coefficients in $\underline{\Pi}'$ and $\underline{\Omega}'$ are provided in the Appendix.

[3] Nevertheless individual forces contributing to the resultant $\boldsymbol{F}$ may act on either the geometrical center G or the barycenter C.

[4] Assume the Jeffery traction to depend on the reference point. Then we have $\boldsymbol{T}^{\mathrm{j}} = \int_{\partial\mathcal{E}} \bar{\boldsymbol{r}}_{\mathrm{P}} \times \tilde{\boldsymbol{t}} \, da = \int_{\partial\mathcal{E}} \left[\bar{\boldsymbol{r}}_{\mathrm{P}} - \bar{\boldsymbol{r}}_{\mathrm{C}}\right] \times \tilde{\boldsymbol{t}} = \underbrace{\int_{\partial\mathcal{E}} \bar{\boldsymbol{r}}_{\mathrm{P}} \times \tilde{\boldsymbol{t}} \, da}_{\boldsymbol{T}^{\mathrm{j}}} - \bar{\boldsymbol{r}}_{\mathrm{C}} \times \underbrace{\int_{\partial\mathcal{E}} \tilde{\boldsymbol{t}} \, da}_{\boldsymbol{0}} = \boldsymbol{T}^{\mathrm{j}}$, see Fig. 3 The result then proves $\boldsymbol{T}^{\mathrm{j}}$ as independent of the reference point.

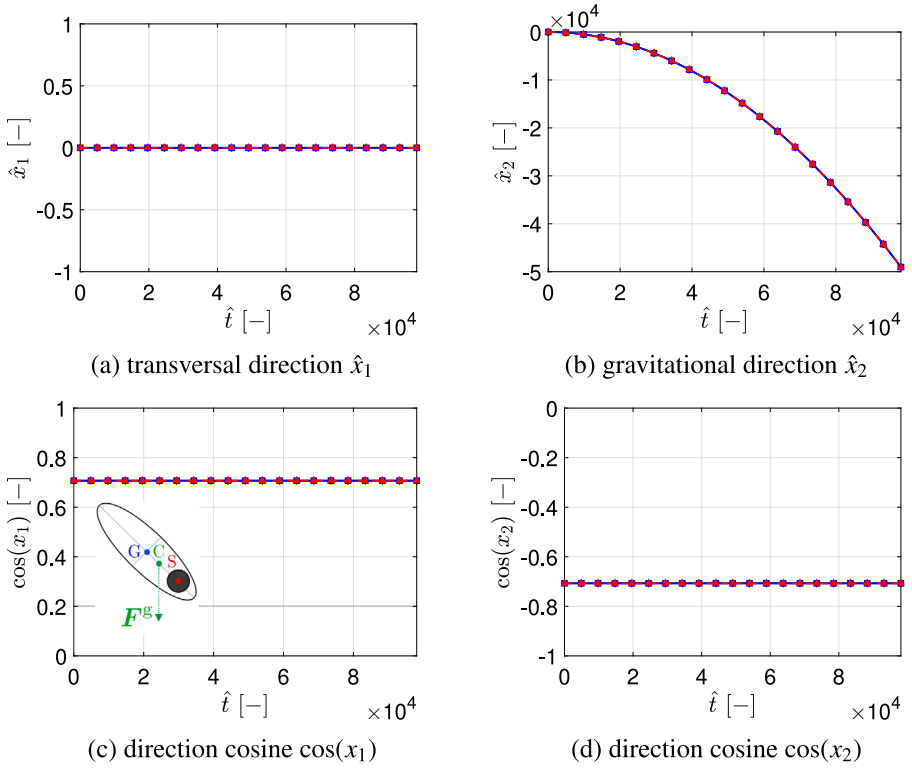

Fig. 5. Gravitational settling of prolate spheroids with $\lambda = 6$ and volume-equivalent diameter $d_{eq} = 1\,\mu m$ in vacuum. The initial orientation is $\varphi_1 = -45°$, $\varphi_2 = \varphi_3 = 0°$. The spherical inclusion has size of $d_s = 0.2 d_{eq}$, density ratio $\hat{\rho} = \rho_s/\rho_e = 1.25$ and is positioned at $\tilde{r}_s = [0.8\,a_1,\ 0,\ 0]$. Note that the displayed position always denotes the geometric center position (x_i, $i = 1,\ 2,\ 3$). Employed nondimensional parameters $\hat{x}_i = x_i/d_{eq}$, $i = 1,\ 2$ and $\hat{t} = t v_{ref}/d_{eq}$. Here, v_{ref} is obtained using $v_{ref} = t_{max} g$, where $t_{max} = 0.1\,s$ and $g = 9.81\ m/s^2$. Comparison of: geometric center formulation, barycenter formulation, homogeneous ellipsoid ($\hat{\rho} = 1$).

3. Demonstrative examples

In this section, the equivalence of the formulations of the Eqs. ((26), (27)) with respect to the geometrical center and with respect to the barycenter is demonstrated on two simple cases.

3.1. Settling in vacuum

In our first validation case, we employ prolate spheroids that settle in vacuum. Thus, the only force acting on the particle under investigation is gravity. Note that the direction of gravity is in the x_2 direction. As the conservation of angular momentum states, the momentum of a rotating object does not change unless it is subjected to an external torque. Consequently, both homogeneous and inhomogeneous particles should preserve their initial angular velocity of zero. In this context, we investigate both the geometric center formulation, as well as the barycenter formulation, see Section 2.4. The density ratio of the spherical inclusions is set to $\hat{\rho} = \rho_s/\rho_e = 1.25$, where the homogeneous particle density is $\rho_e = 2560\,kg/m^3$. The aspect ratio of the prolate spheroid is chosen as $\lambda = 6$ and the volume-equivalent diameter of the particles as $d_{eq} = 1\,\mu m$. The spherical inclusion is located at $\tilde{r}_s = [0.8\,a_1,\ 0,\ 0]$ and has a diameter of $d_s = 0.2 d_{eq}$. The initial Euler angles are set to $\varphi_1 = -45°$, $\varphi_2 = \varphi_3 = 0°$.

As displayed in Fig. 5 (a–b), the trajectory of the homogeneous particle is identical to that of the inhomogeneous particles (barycenter and geometric center formulation). Moreover, we observe an excellent agreement between the barycenter and geometrical center formulation. As shown in Fig. 5 (c–d), the particle's initial orientation is preserved (no rotation during settling) while settling in vacuum as they are initialized with a zero angular velocity and are not subjected to any external torque during settling.

3.2. Settling in air

Next, we examine inhomogeneous, prolate spheroids that settle in air. The predominant forces acting on the particle under investigation are therefore gravity and drag force. The particles used have the same properties as in Section 3.1. With density $\rho_f = 1.208\ kg/m^3$ and kinematic viscosity $\nu_f = 1.491e\text{-}05\ m/s^2$ of air, we obtain a terminal velocity of the corresponding homogeneous particle of $v_t = 7.7426e\text{-}05\ m/s$ (see Eq. (14)), resulting in a maximum particle Reynolds number of $Re_{p\,max} = 5e\text{-}06 \ll 1$.

As before, we compare both the center of gravity and the barycenter formulation, where the position compared is always the geometric center (x_i, $i = 1,\ 2,\ 3$). The following two initial orientations are examined: $\varphi_1 = \pm 45°$, $\varphi_2 = \varphi_3 = 0°$.

As presented in Fig. 6 (a–d), we observe strong differences between the homogeneous particle and the inhomogeneous particles (geometrical and barycenter formulation) in both translational and orientational dynamics. While the homogeneous particle travels in the observed time $\hat{t} \approx 5800$ for $711\,d_{eq}$ in x_1, the inhomogeneous particle only reaches $133\,d_{eq}$ in x_1, see Fig. 6 (a). In addition, the inhomogeneous particle travels $667\,d_{eq}$ further in the direction of gravity, see Fig. 6 (b). These differences in trajectory are caused by the altered particle orientation as shown in Fig. 6 (c,d). As displayed, the homogeneous particle remains in its original orientation during settling, while the inhomogeneous particle aligns the longitudinal particle axis with the gravitational direction, thus reducing the acting drag force. Moreover, we observe a perfect agreement between the barycenter and the formulation of the geometric center.

Next, we inject the particle with $\varphi_1 = +45°$, $\varphi_2 = \varphi_3 = 0°$ and analyze the effects on the translational and orientational dynamics due to an altered initial orientation. Fig. 7 (a,b) illustrates the strong influence of the spherical inclusion on the particle trajectory, which is a result of the change in the orientation dynamics of the particles, see

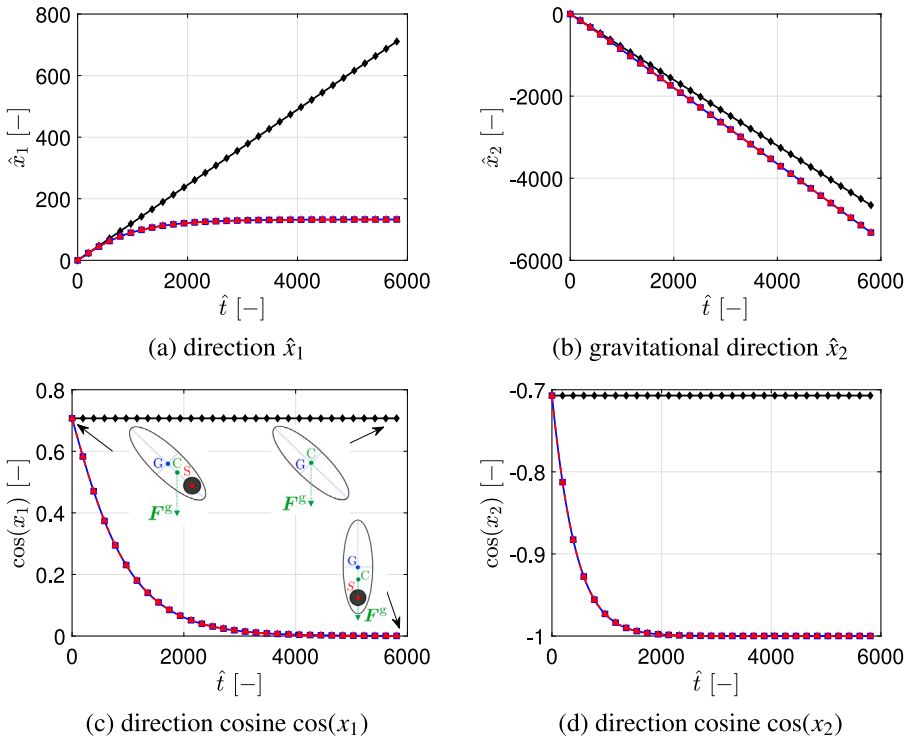

Fig. 6. Gravitational settling of prolate spheroids with $\lambda = 6$ and volume-equivalent diameter $d_{eq} = 1\,\mu m$ in air. The initial orientation is $\varphi_1 = -45°$, $\varphi_2 = \varphi_3 = 0°$. The spherical inclusion has size of $d_s = 0.2d_{eq}$, density ratio $\hat{\rho} = \rho_s/\rho_e = 1.25$ and is positioned at $\tilde{r}_s = [0.8\,a_1,\ 0,\ 0]$. Note that the displayed position always denotes the geometric center position (x_i, $i = 1,\ 2,\ 3$). Employed nondimensional parameters $\hat{x}_i = x_i/d_{eq}$, $i = 1,\ 2$ and $\hat{t} = tv_t/d_{eq}$ with v_t for the homogeneous particle ($\hat{\rho} = 1$) from Eq. (14). Comparison of: geometric center formulation, barycenter formulation, homogeneous ellipsoid ($\hat{\rho} = 1$).

Fig. 7 (c,d). As shown in Fig. 7 (c,d) ($\varphi_1 = +45°$), we observe a change in the orientation dynamics between homogeneous and inhomogeneous particles compared to Fig. 6 (c,d) ($\varphi_1 = -45°$), which is caused by the modified initial orientation. However, regardless of the changed initial orientation, the inhomogeneous particles reach a stable orientation of the particle's major axis at $\hat{t} \approx 4000$ that coincides with the gravitational direction. As displayed, the homogeneous particle remains again in its initial orientation. Moreover, we observe a perfect agreement between the barycenter and the geometric center formulation, also for the altered initial position.

Taken together, both the barycenter and center of geometry formulation are equivalent and are considered validated. In the upcoming examples, only the geometrical center formulation is used for the simulations.

4. Results and discussion

4.1. Influence of different inclusion densities

In the following, the motion of inhomogeneous prolate ellipsoids with aspect ratio $\lambda = 12$ is investigated when settling in air. The volume-equivalent diameter of the particles is set to $d_{eq} = 1\ \mu m$ ($Re_{p\,max} = 5e\text{-}06 \ll 1$) while the spherical inclusion for all considered particles is located at $\tilde{r}_s = [0.6\,d_{eq},\ 0,\ 0]^t$ in the pFoR and has diameter $d_s = 0.2d_{eq}$. The initial particle position is $[0,\ 0,\ 0]^t$ in the iFoR, while the initial particle orientation is chosen as $\varphi_1 = -45°$, $\varphi_2 = \varphi_3 = 0°$. For the inclusion, a density ratio $\hat{\rho} = \rho_s/\rho_e$ in the range of $\hat{\rho} = [1,\ 1.25,\ 1.5\ ,2\ ,\ 2.5,\ 5]$ is chosen. The particle is tracked for $t = 2\,s$. Fig. 8 (a–d) presents both the orientation dynamics and translational dynamics. As shown in Fig. 8 (a,b), the orientation dynamics is strongly influenced by the inclusion density ratio $\hat{\rho} = \rho_s/\rho_e$. We observe that the greater $\hat{\rho}$, the faster the particle aligns its long axis with the gravitational direction and the faster the angular velocity decreases, see Fig. 8(d). In addition, the faster the particle aligns with the direction of gravity, the less the particle travels in $\hat{x}_1$ and the greater the settling of the particle in $\hat{x}_2$. Note that the motion in $\hat{x}_1$ is a consequence of a non-aligned particle as the drag force acting on the particle possesses a contribution both in $\hat{x}_1$ and $\hat{x}_2$.

4.1.1. Influence of various aspect ratios with identical inclusion position

In the following we investigate the motion of inhomogeneous prolate ellipsoids of various aspect ratios, i.e. $\lambda = 1.5,\ 3,\ 6,\ 12$, when settling in air. The volume-equivalent diameter of the particles is set to $d_{eq} = 1\ \mu m$, while the spherical inclusion for all particles considered is positioned at $\tilde{r}_s = [0.6\,d_{eq},\ 0,\ 0]^t$ in the pFoR and has diameter $d_s = 0.2d_{eq}$. The initial particle position is $[0,\ 0,\ 0]^t$ in the iFoR, while the initial particle orientation is chosen as $\varphi_1 = -45°$, $\varphi_2 = \varphi_3 = 0°$. A density ratio $\rho_s/\rho_e = 1.5$ is employed for the spherical inclusion. The particle is tracked for $t = 2\,s$.

As presented in Fig. 9 (a,b), all particles with inclusions ($\rho_s \neq \rho_e$) reach the same final orientation, while the homogeneous particles maintain their original orientation. We further observe that more elongated particles take more time to reach the final particle orientation, which is caused by an initial lower particle angular velocity, see Fig. 9 (d). Note that the slower alignment of the long axis with the gravitational direction directly affects the trajectory of the particle, see Fig. 9 (c), where the more elongated particles travel significantly farther in the $\hat{x}_1$ direction. Here, we include two homogeneous reference ellipsoids with aspect ratio $\lambda = 1.5, 12$. Furthermore, Fig. 9 (c) highlights that all considered inhomogeneous particles travel less in the $\hat{x}_1$ direction than their homogeneous counterparts. While the homogeneous particle with aspect ratio $\lambda = 12$ reaches $\hat{x}_1 \approx 947$, the inhomogeneous particle with $\lambda = 12$ only travels up to $\hat{x}_1 \approx 410$. Note that due to the alignment with the gravitational direction, the considered inhomogeneous particles with $\lambda < 6$ travel less far in $\hat{x}_1$ than the homogeneous reference ellipsoid with $\lambda = 1.5$.

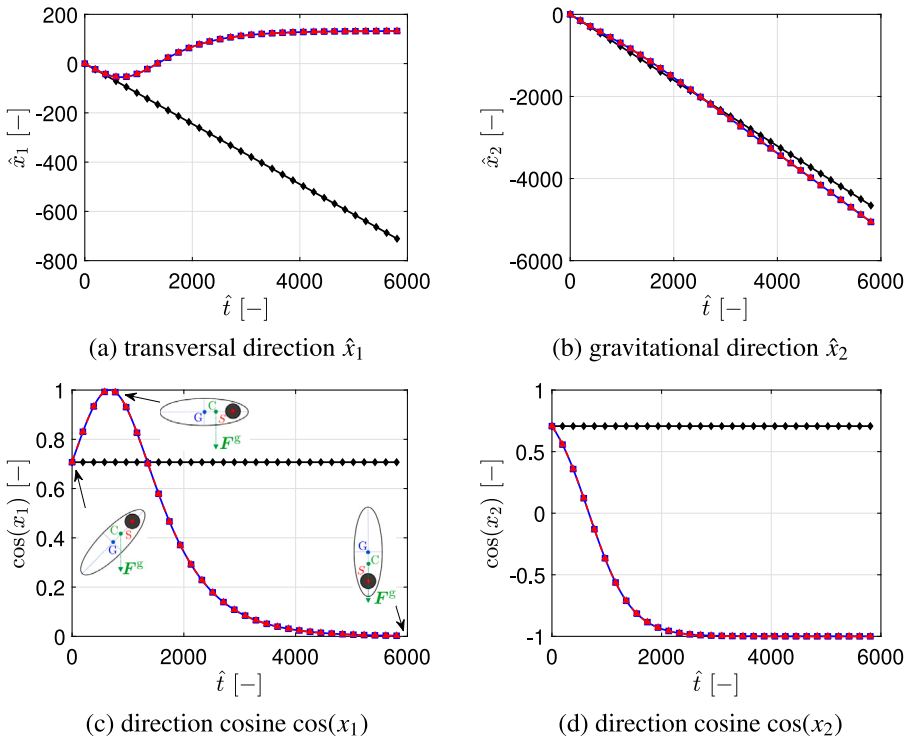

Fig. 7. Gravitational settling of prolate spheroids with $\lambda = 6$ and volume-equivalent diameter $d_{eq} = 1\,\mu m$ in air. The initial orientation is $\varphi_1 = +45°,\ \varphi_2 = \varphi_3 = 0°$. The spherical inclusion has size of $d_s = 0.2 d_{eq}$, density ratio $\hat{\rho} = \rho_s/\rho_e = 1.25$ and is positioned at $\hat{r}_s = [0.8\,a_1,\ 0,\ 0]$. Note that the displayed position always denotes the geometric center position ($x_i,\ i = 1,\ 2,\ 3$). Employed nondimensional parameters $\hat{x}_i = x_i/d_{eq},\ i = 1,\ 2$ and $\hat{t} = t v_t/d_{eq}$ with v_t for the homogeneous particle ($\hat{\rho} = 1$) from Eq. (14). Comparison of: geometric center formulation, barycenter formulation, homogeneous ellipsoid ($\hat{\rho} = 1$).

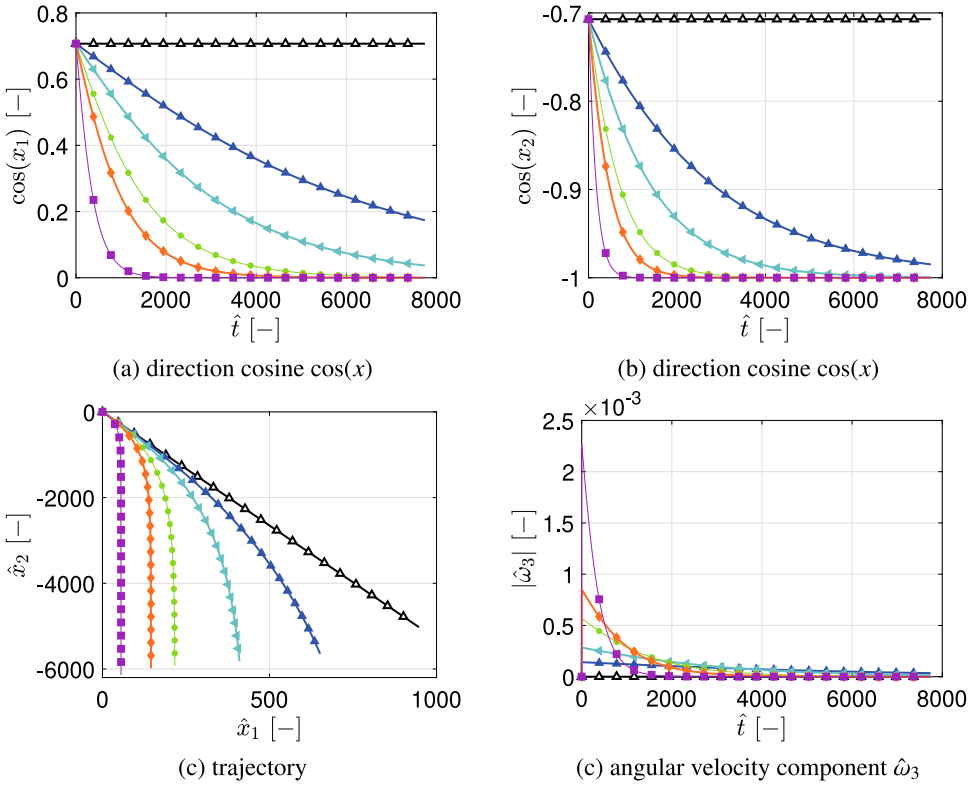

Fig. 8. Gravitational settling of homogeneous and non-homogeneous prolate ellipsoids with initial orientation $\varphi_1 = -45°, \varphi_2 = \varphi_3 = 0°$ of various spherical inclusion density ratios $\hat{\rho}$. The spherical inclusion is positioned at $\hat{r}_s = [0.6\,d_{eq},\ 0,\ 0]'$. Employed nondimensional parameters $\hat{x}_i = x_i/d_{eq},\ i = 1,\ 2$ and $\hat{t} = t v_t/d_{eq}$ with v_t for the homogeneous particle ($\hat{\rho} = 1$) from Eq. (14). Investigated $\hat{\rho}$: 1 (hom.), 1.25, 1.5, 2, 2.5, 5.

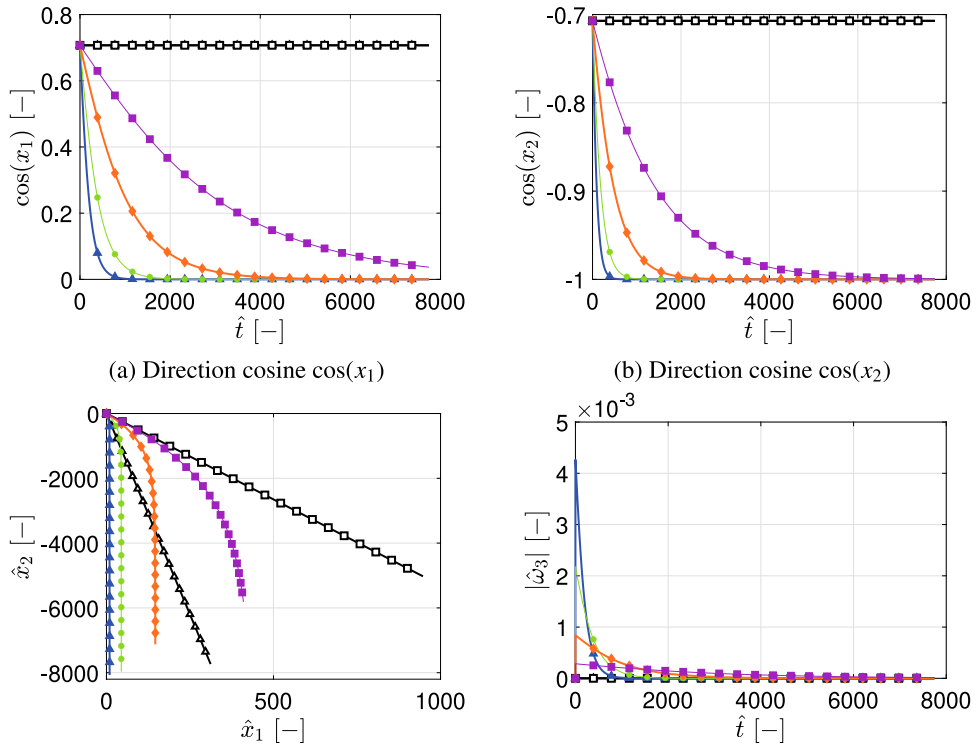

(a) Direction cosine $\cos(x_1)$ (b) Direction cosine $\cos(x_2)$

Fig. 9. Gravitational settling of homogeneous and non-homogeneous prolate ellipsoids with initial orientation $\varphi_1 = -45°, \varphi_2 = \varphi_3 = 0°$ of various aspect ratios (λ). The spherical inclusion is positioned at $\tilde{r}_s = [0.6\,d_{eq},\ 0,\ 0]^t$. Employed nondimensional parameters $\hat{x}_i = x_i/d_{eq},\ i = 1,\ 2$ and $\hat{t} = tv_t/d_{eq}$ with v_t for the homogeneous particle ($\hat{\rho} = 1$) from Eq. (14). Homogeneous ellipsoid references with λ: △1.5, □12. Inhomogeneous ellipsoids with λ: 1.5, 3, 6, 12.

4.1.2. *Influence of various aspect ratios with varying inclusion position*

In this example, the spherical inclusion size and density ratio is identical to the previous section, however, the inclusion positioned in the pFoR is chosen as $[0.8\,a_1,\ 0,\ 0]$ and thus varies with changing particle aspect ratio. By comparing Fig. 10 (a–b) to Fig. 9 (a–b) (Section 4.1.1), we observe that for particles with an increased offset of the spherical inclusion from the geometrical center, the alignment of the particle long axis with the gravitational direction is reached significantly faster. For example the particle with $\lambda = 12$ and particle inclusion at $\tilde{r}_s = [0.8\,a_1,\ 0,\ 0]^t$ aligns its major axis with the gravitational direction at $\hat{t} \approx 4000$, while the particle investigated in Section 4.1.1 with $\lambda = 12$ and particle position at $\tilde{r}_s = [0.6\,d_{eq},\ 0,\ 0]^t$ aligns at $\hat{t} > 8000$. This is also highlighted by an increased particle angular velocity of the more elongated particles such as $\lambda > 1.5$, see Fig. 10 (d) compared to Fig. 9 (d). This faster alignment strongly impacts also the particle trajectory as presented in Fig. 10 (c), where the inhomogeneous particles, due to their faster alignment with the flow, travel less in $\hat{x}_1$ and further in $\hat{x}_2$.

4.2. *Effect of inclusion properties on the orientational motion*

To study the overall effect of the inhomogeneity on the orientational dynamics, a parameter variation of different aspect ratios, particle inclusion positions, and inclusion diameters was conducted. A matrix of simulations of the gravitational settlement of a particle with a constant $d_{eq} = 1$ µm ($\mathrm{Re}_{p\,max} = 5\mathrm{e}{-06} \ll 1$) for aspect ratios $\lambda \in [1.5, 12]$, inclusion radii $r_s \in [0.1a_2, 0.9a_2]$ and inclusion positions $\tilde{r}_s \in [0.1a_1, 0.9a_1]$ was performed for a non-dimensional time of $\hat{t} = 500$. The initial orientation was the same as employed in the previous sections, i.e. $\varphi_1 = -45°$, $\varphi_2 = \varphi_3 = 0°$. The density ratio is kept at $\hat{\rho} = \rho_s/\rho_e = 1.5$ for all cases. The final orientation at $\hat{t} = 500$ is depicted in Fig. 11. We observe a decreasing value of the direction cosine $\cos(x_1)$ with a larger orientational change as the initial direction cosine was set to $\cos(x_1) = 0.707$. As demonstrated in previous cases, a small impact on the rotation of particles with small inclusion diameters and increasing aspect ratio is observed. Particles with large inclusion diameter and large inclusion offset are almost aligned to the gravitational direction having the direction cosine below $\cos(x_1) = 0.1$. The highest density of the isosurfaces in the direction of $\hat{r}_s$ causes the highest impact of the considered variables on the rotational motion.

To better visualize the effect of these variables on the trajectory, several plane sections of the 3D plot in Fig. 11 are created and presented in the following. In Fig. 12 the final orientation for different inclusion radii and offset for two aspect ratios of 6 and 12 is depicted. Comparing both plots shows that the particle with a higher aspect ratio and the same inclusion parameters rotates less. The higher slope of the contours for small values of normalized inclusion position $\tilde{r}_s/a_1$ indicates a greater impact on the rotation. We observe that the sensitivity of the orientational dynamics on the inclusion position is increasing for larger inclusions. Note that increasing the inclusion size, i.e. the inclusion radius, impacts the trajectory stronger than enlarging the inclusion offset in the whole range.

Interesting observations are made when fixing the position $\tilde{r}_s/a_1$ of the inclusion. Fig. 13 presents dependence of the final orientation on the aspect ratio λ and normalized inclusion radius r_s/a_2. Shifting the inclusion towards the top ($\tilde{r}_s/a_1 \uparrow$) results in a faster rotation due to a higher gravity torque which is in agreement with intuition. Analyzing the shape of the contours yields that the relation between the aspect ratio and inclusion radius is almost linear. Thus, to maintain a constant rotational motion for a given inclusion position, the ratio between λ and inclusion radius (r_s/a_2) has to be approximately constant.

In Fig. 14 the final state of particles with equal normalized inclusion size r_s/a_2 for different aspect ratios and positions of the inclusion ($\tilde{r}_s/a_1$) are shown. As observed, a higher inclusion radius results in a faster rotation, thus the values of the direction cosine are lower. To obtain the same rotational motion with increasing aspect ratio the inclusion must be shifted to the top along the contour lines. However, note the nonlinear relationship.

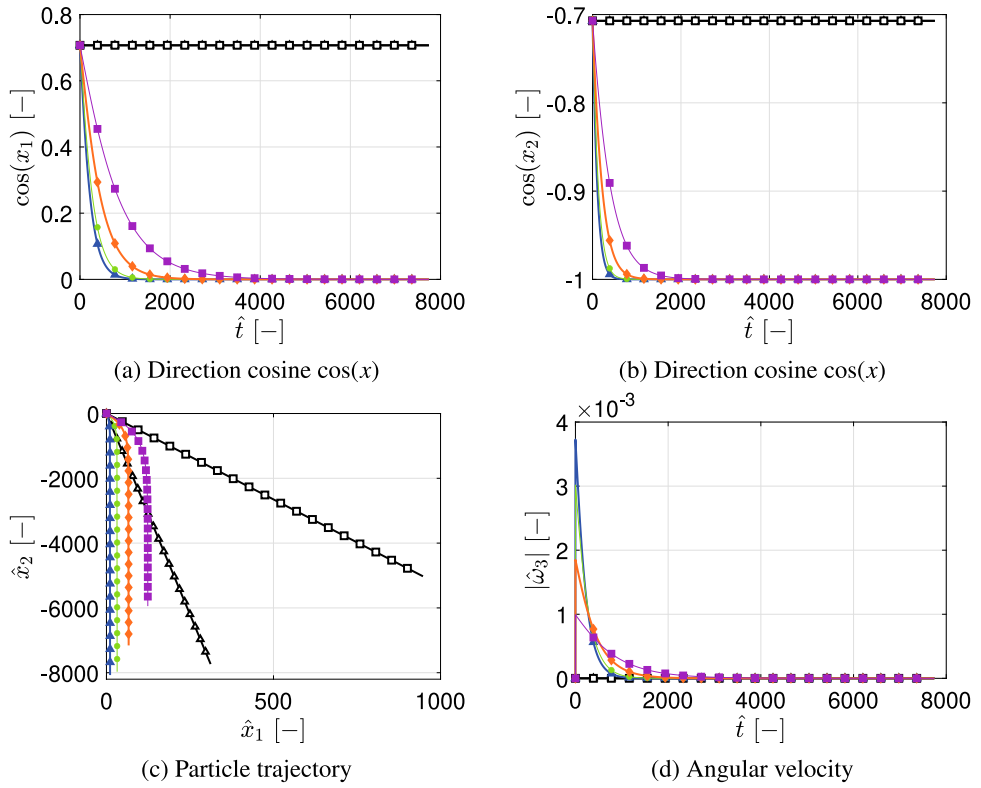

(a) Direction cosine $\cos(x)$ (b) Direction cosine $\cos(x)$

(c) Particle trajectory (d) Angular velocity

Fig. 10. Gravitational settling of homogeneous and non-homogeneous prolate ellipsoids with initial orientation $\varphi_1 = -45°, \varphi_2 = \varphi_3 = 0°$ of various aspect ratios. The spherical inclusion is positioned at $\underline{\tilde{r}}_s = [0.8a_1,\ 0,\ 0]$. Employed nondimensional parameters $\hat{x}_i = x_i/d_{eq}$, $i = 1,\ 2$ and $\hat{t} = tv_t/d_{eq}$ with v_t for the homogeneous particle ($\hat{\rho} = 1$) from Eq. (14). Homogeneous ellipsoid references λ: △ 1.5, □ 12. Inhomogeneous ellipsoids λ: 1.5, 3, 6, 12.

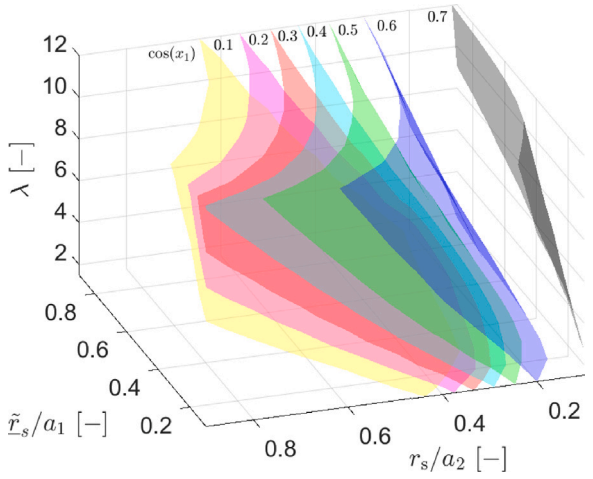

Fig. 11. Isosurfaces of $\cos(x_1)$ for $\hat{t} = 500$ visualized dependent on the aspect ratio λ, the normalized inclusion position $\underline{\tilde{r}}_s/a_1$ and the normalized inclusion radius r_s/a_2.

4.3. Simple shear flow

Next, we insert a prolate spheroid of $\lambda = 20$ in simple shear flow. Recall that simple shear flow has rotational ($\underline{w}_f$) and shearing contributions ($\underline{d}_f$). Thus, the fluid velocity gradient $\nabla\underline{u}$ can be expressed as follows:

$$\nabla\underline{u} = \begin{bmatrix} 0 & \dot{\gamma} & 0 \\ 0 & 0 & 0 \\ 0 & 0 & 0 \end{bmatrix} = \underbrace{\begin{bmatrix} 0 & \dot{\gamma}/2 & 0 \\ \dot{\gamma}/2 & 0 & 0 \\ 0 & 0 & 0 \end{bmatrix}}_{\underline{d}_f} + \underbrace{\begin{bmatrix} 0 & \dot{\gamma}/2 & 0 \\ -\dot{\gamma}/2 & 0 & 0 \\ 0 & 0 & 0 \end{bmatrix}}_{\underline{w}_f}, \tag{48}$$

where $\dot{\gamma}$ denotes the shear rate. We choose $\dot{\gamma} = +726\,\mathrm{s}^{-1}$ and investigate two initial orientations, i.e $\varphi_1 = \pm 90°$, $\varphi_2 = \varphi_3 = 0°$. In contrast to the previous sections we will investigate the impact of the mass ratios (inclusion size and density impact combined) on the translational and orientational dynamics, which is defined as $\hat{m} = \Delta m_s/m_e = [0.05,\ 0.1,\ 0.15,\ 0.2]$ with $\rho_e = 2560\,\mathrm{kg/m}^3$. The particle inclusion is located at $\underline{\tilde{r}}_s = [0.8a_1,\ 0,\ 0]^t$ and is of size $d_s = 0.15\,d_{eq}$.

As shown in Fig. 15 (a–d), the orientation dynamics of the prolate spheroids are strongly influenced by the inclusion density. It is shown that the higher the spherical density inclusion, the longer the time until the particle undergoes a full rotation. Thus, these particles possess a smaller particle flipping frequency. Furthermore, Fig. 15 (a–d) indicates that there is a critical particle mass ratio $\hat{m}_{crit}$ in the range of $0.1 < \hat{m}_{crit} < 0.15$, where the particle nearly aligns with the flow direction and no further particle flips are visible in the observed time. This stable orientation could be identified as an equilibrium state where the sum of all torques is zero. Moreover, we observe that for particles with $\hat{m} > \hat{m}_{crit}$, the initial orientations of $\varphi_1 = \pm 90°$ lead to identical particle orientation, thus the initial injection orientation of the considered cases plays a negligible role for $\hat{m} > \hat{m}_{crit}$. Taken together, particles with increasing $\hat{m}$ drift away from the (homogeneous) Jeffery orbit by exhibiting a significant effect on the period of rotation, until finally reaching a stable orientation at $\hat{m} \to \hat{m}_{crit}$. Thus (homogeneous) Jeffery orbits are not able to describe the rotational dynamics of inhomogeneous particles.

In the following, we investigate the dependency of the flipping time t_{flipp} of the particles on the spherical mass inclusion ratio $\hat{m} = \Delta m_s/m_e$ for four different aspect ratios ($\lambda = 10,\ 15,\ 20,\ 25$), three different inclusion diameters ($\hat{d} = d_s/d_{eq} = 0.075,\ 0.15,\ 0.3$) as well a varying inclusion positions on the particle semi-major axis $\hat{\tilde{r}}_{s1} = \tilde{r}_{s1}/a_1$. Note that in this linear shear flow example, we define the nondimension flipping time depending on the shear rate $\dot{\gamma}$, i.e. $\hat{t}_{flipp} = t_{flipp}/t_{ref}$ with $t_{ref} = 1/|\dot{\gamma}|$. As displayed in Fig. 16 (a,b), we observe that increasing

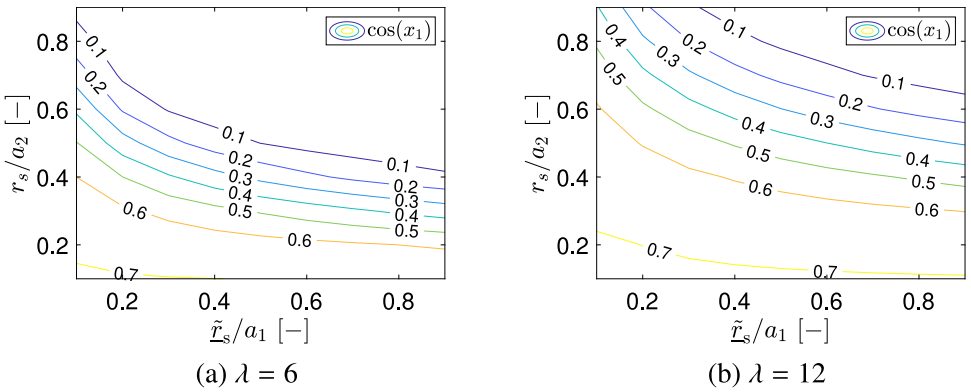

Fig. 12. $\cos(x_1)$ for $\hat{t} = 500$ visualized in dependence on normalized inclusion position $\tilde{r}_s/a_1$ and normalized inclusion radius r_s/a_2 for aspect ratio $\lambda = 6$ (a) and $\lambda = 12$ (b).

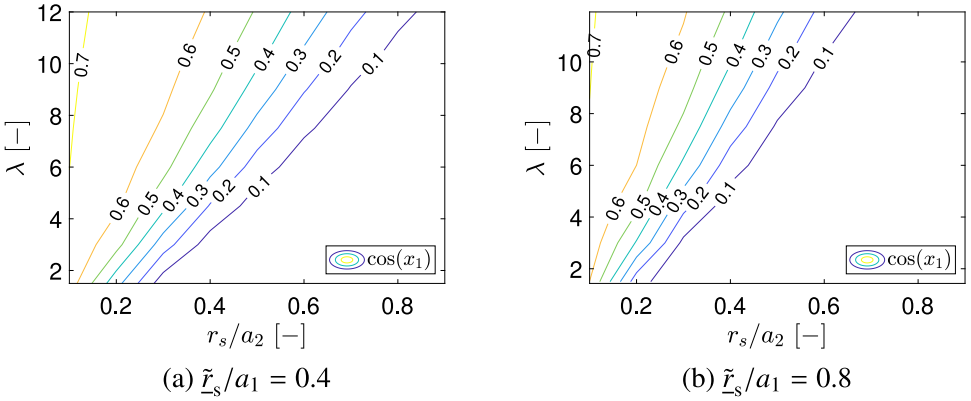

Fig. 13. $\cos(x_1)$ for $\hat{t} = 500$ visualized dependent on the aspect ratio λ and normalized inclusion radius r_s/a_2 for the normalized inclusion position $\tilde{r}_s/a_1 = 0.4$ (a) and $\tilde{r}_s/a_1 = 0.8$ (b).

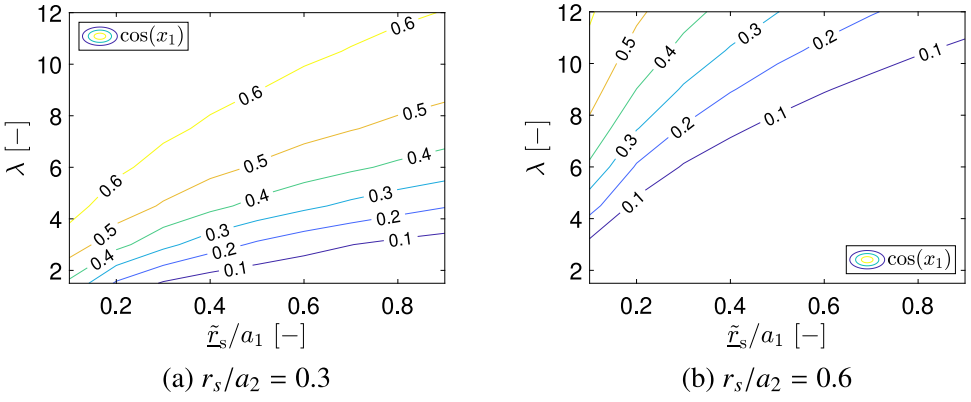

Fig. 14. $\cos(x_1)$ for $\hat{t} = 500$ visualized dependent on aspect ratio λ and normalized inclusion position $\tilde{r}_s/a_1$ for normalized inclusion radius $r_s/a_2 = 0.3$ (a) and $r_s/a_2 = 0.6$ (b).

$\hat{m}$ increases $\hat{t}_{\mathrm{flipp}}$ significantly for all particles investigated. In addition, we find that increasing the particle aspect ratio significantly reduces the $\hat{m}_{\mathrm{crit}}$, where $\hat{t}_{\mathrm{flipp}} \to \infty$. Thus, a more elongated particle tends to reach for lower inclusion masses a nonrotating state than a less elongated particle with equal inclusion mass. Furthermore, we observe that increasing d_s and thus distributing the inclusion mass over a larger volume (i.e. a smaller density), leads to an increase in $\hat{t}_{\mathrm{flipp}}$. Moreover, we find that increasing the shift of the spherical inclusion from the geometrical center of the particle leads to a strong decrease in $\hat{t}_{\mathrm{flipp}}$, see Fig. 16 (b).

4.4. Laminar pipe flow

Next, we investigate the particle motion of an inhomogeneous prolate ellipsoid in laminar pipe flow. The setup is consistent with the setup employed in Wedel et al. [30] and Cui et al. [35]. The circular channel has diameter $D = 4.2\,\mathrm{mm}$ and mean velocity $\bar{U} = 0.485\,\mathrm{m/s}$, [36]. The studied prolate spheroid has a density of $\rho_s = 2560\,\mathrm{kg/m^3}$ and aspect ratio of $\lambda = 14$ with semi-minor axis $a_3 = 0.5\,\mu\mathrm{m}$ leading to $d_{\mathrm{eq}} = 2.41\mathrm{e}{-06}$. The Reynolds number is $\mathrm{Re} = 137$ (density $\rho_f = 1.208\,\mathrm{kg/m^3}$, kinematic viscosity $\nu_f = 1.491 \times 10^{-5}\,\mathrm{m^2/s}$). Note that $\rho_s \gg \rho_f$. Furthermore, $\mathrm{Stk} = 0.01$ with characteristic particle

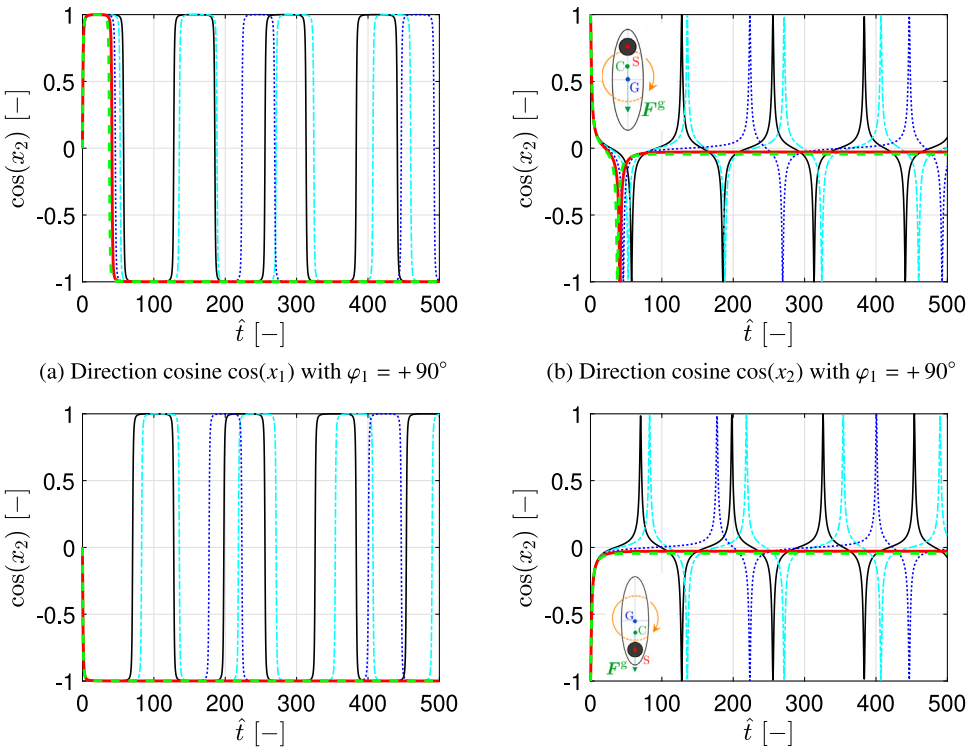

(a) Direction cosine $\cos(x_1)$ with $\varphi_1 = +90°$ (b) Direction cosine $\cos(x_2)$ with $\varphi_1 = +90°$

(c) Direction cosine $\cos(x_1)$ with $\varphi_1 = -90°$ (d) Direction cosine $\cos(x_2)$ with $\varphi_1 = -90°$

Fig. 15. Motion of prolate spheroidal ellipsoid ($\lambda = 20$) in simple shear flow ($\dot{\gamma} = 726\,\mathrm{s}^{-1}$) with varying mass ratio of the inclusion. The spherical inclusion is of size $d_s = 0.15\,d_{eq}$ and the inclusion position is $[0.8a_1,\ 0,\ 0]$. The initial particle orientation is set to $\varphi_1 = \pm 90°,\ \varphi_2 = 0°,\ \varphi_3 = 0°$. The hydrodynamic torque acting on the particle in the initial configuration is sketched using an orange arrow. Employed nondimensional parameter $\hat{t} = t|\dot{\gamma}|$. Mass ratios $\hat{m} = \Delta m_s/m_e$: 0 (hom.), 0.05, 0.1, 0.15, 0.2.

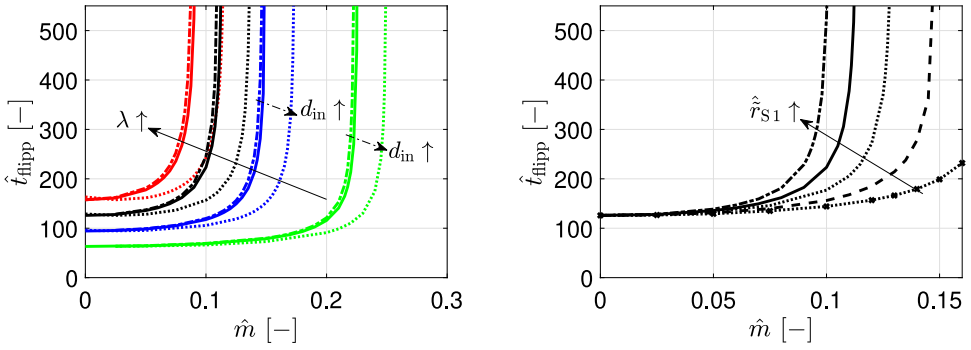

(a) Inclusion position $\underline{\tilde{r}}_s = [0.8a_1,\ 0,\ 0]^T$ (b) Aspect ratio $\lambda = 20$ and $d_s = 0.15\,d_{eq}$

Fig. 16. Influence of particle aspect ratios λ, spherical inclusion size d_{in} and inclusion position on the particle semi-major axis $\tilde{r}_{s1}$ on the particle flipping time $\hat{t}_{flipp}$. The homogeneous density of the ellipsoid matrix is $\rho_e = 2560\,\mathrm{kg/m^3}$ and the volume-equivalent diameter is set to $d_{eq} = 1$ µm. Employed nondimensional parameter $\hat{t} = t|\dot{\gamma}|$ and $\hat{m} = \Delta m_s/m_e$. Studied aspect ratios λ in (a): 10, 15, 20, 25 and particle inclusion size $\hat{d} = d_{in}/d_{eq}$: 0.075, 0.15, 0.3. Studied spherical inclusion position $\hat{\tilde{r}}_{s1} = \tilde{r}_{s1}/a_1$ in (b): 0.9, 0.8, 0.7, 0.6, 0.5.

response time $\tau_p = 0.046\,\mathrm{ms}$. The initial position of the ellipsoid is set to $x_2(0) = -1.65\,\mathrm{mm}$ in the plane $e_1 - e_2$ and its initial orientation is chosen as $\varphi_1 = -90°,\ \varphi_2 = \varphi_3 = 0°$. At the initial particle position, the flow vorticity is $\omega_f = 726\,\mathrm{s}^{-1}$. The initial velocity and angular velocity of the particle are set to zero. Thus, we can estimate the maximum particle Reynolds number of $\mathrm{Re}_{p\,max} = 0.08$. Note that this $\mathrm{Re}_{p\,max}$ only occurs directly at the beginning of the simulation as the initial particle velocity is set to zero. Thus, throughout the simulation $\mathrm{Re}_p \ll 1$ For convenience, the setup is visualized in Fig. 17.

First, we compare the developed particle tracking of prolate ellipsoids with spherical inclusions with the numerical results of Tian et al. [19] and Cui et al. [35] in the limit of homogeneous particles ($\rho_{in} = \rho_{hom}$) with aspect ratio $\lambda = 14$. As shown in Fig. 18, we achieve a perfect agreement in the orientation dynamics with the reported results of Cui et al. [35], who assumed an average inflow velocity of $\bar{U} = 0.485\,\mathrm{m/s}$.

Next, we employ several mass inclusions with $\hat{m} = 0$ (hom.), 0.025, 0.05, 0.1 with inclusion diameter $d_s = 0.15\,d_{eq}$. To neglect the gravity influence on the particle trajectory, the particle mass is kept constant across all particles, i.e. when considering inclusions the homogeneous mass is adjusted correspondingly.

As presented in Fig. 19 (a–b), the effect on the orientation dynamics for the aspect ratio $\lambda \leq 14$ is notable even for $\hat{m} = 0.025$. Furthermore, we observe that with increasing mass ratio $\hat{m}$, the deviation of the particle orientation from the homogeneous ellipsoid reference increases, which is consistent with our findings in Section 4.3. We observe that $0.05 < \hat{m}_{crit} < 0.1$, as the particle with $\hat{m} = 0.1$ aligns with the flow direction and no further rotational motion is observed.

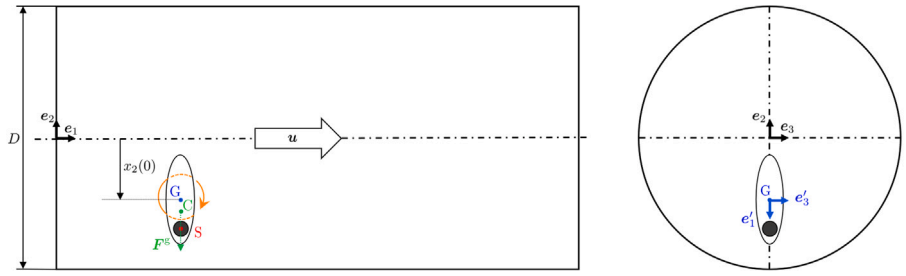

Fig. 17. Sketch of a circular tube of diameter $D = 4.2\,\mathrm{mm}$ and initial position of the inhomogeneous particle in the $e_1 - e_2$ plane. Note the exaggerated size of the suspended prolate ellipsoidal particle for display purposes. The Reynolds number of the airflow is Re = 137 with average inlet velocity $\bar{U} = 0.485\,\mathrm{m/s}$. The streamwise direction is in the e_1 direction, while the gravitational direction points in the negative e_2 direction. The particle is positioned at $x_2(0) = -1.65\,\mathrm{mm}$ out of the center plane in e_2 direction with initial orientation $\varphi_1 = -90°$, $\varphi_2 = \varphi_3 = 0°$. The hydrodynamic torque acting on the particle in the initial configuration is sketched using an orange arrow.

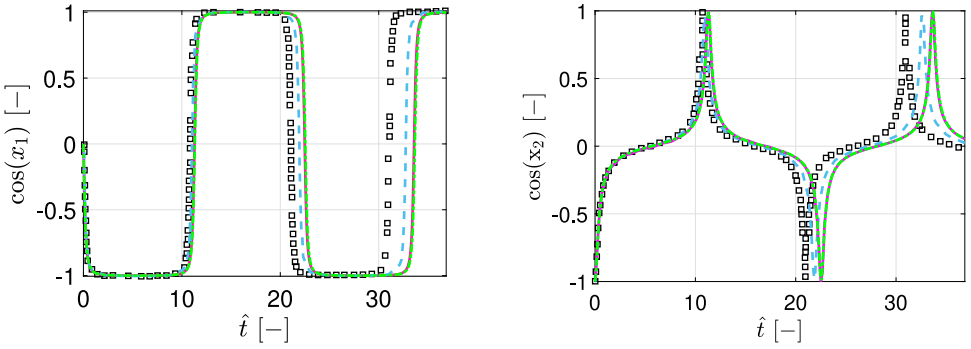

Fig. 18. Particle orientation of homogeneous prolate ellipsoid ($\rho_{in} = \rho_{hom}$) of $\lambda = 14$ of a prolate ellipsoidal particle in laminar pipe flow. Employed nondimensional parameter $\hat{t} = t v_t / d_{eq}$ with v_t for the homogeneous particle ($\hat{\rho} = 1$) from Eq. (14). Reference results from the literature and present model: □ Tian et al. [19], ■ ■ Cui et al. ($\bar{U} = 0.5\,\mathrm{m/s}$) [35], ■ Cui et al. ($\bar{U} = 0.485\,\mathrm{m/s}$), [35], ■ ■ present model ($\bar{U} = 0.485\,\mathrm{m/s}$).

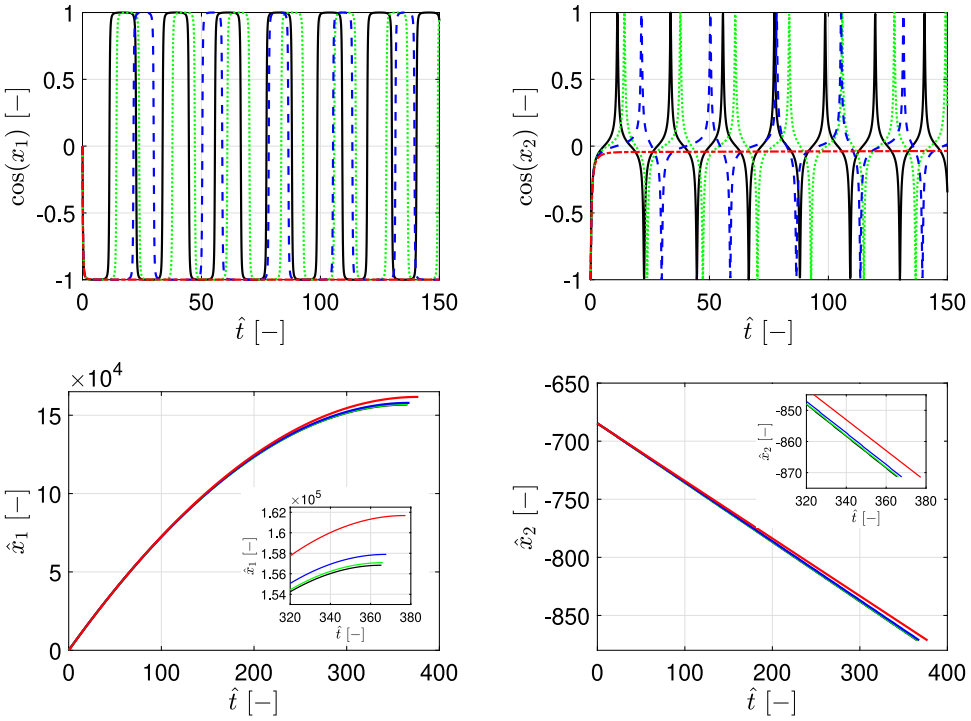

Fig. 19. Particle orientation of inhomogeneous prolate ellipsoids suspended in laminar pipe flow. Employed nondimensional parameter $\hat{t} = t v_t / d_{eq}$ with v_t from Eq. (14) for the homogeneous particle ($\hat{m} = 0$) with particle aspect ratio $\lambda = 14$. Investigation of spherical mass inclusion ratios $\hat{m} = \Delta m_s / m_e$ with inclusion diameter $d_s = 0.15\,d_{eq}$ and inclusion position $\hat{r}_{si} = 0.8\,a_1$. Inclusion mass ratio $\hat{m}$: ■ 0, ■ 0.025, ■ 0.05, ■ 0.1.

Fig. 19 (c,d) shows the influence of the spherical inclusion on the particle trajectory. We observe that a particle with larger mass ratio travels further in streamwise direction (x_1) and possesses a decreased settling velocity in x_2. For example, the particle with $\hat{m} = 0.1$ travels $3788\,d_{eq}$ further in x_1 compared to the particle with $\hat{m} = 0.05$ and $4846\,d_{eq}$ more than the particle without inclusion. The larger afloat time

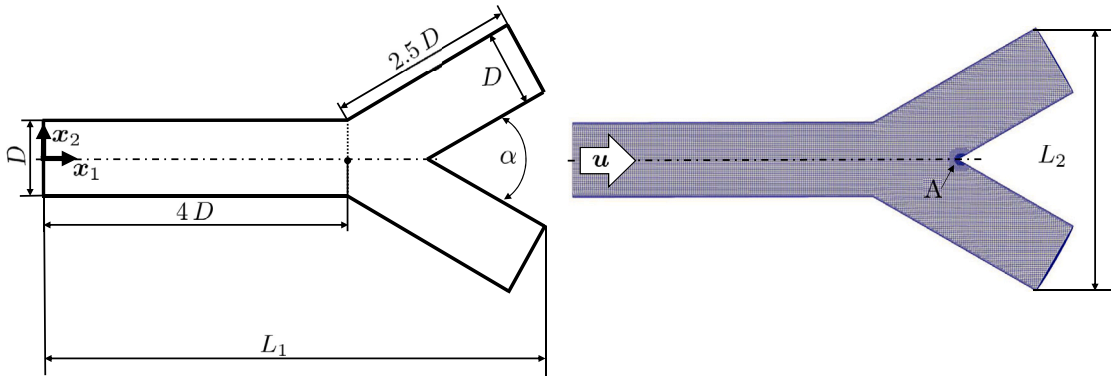

Fig. 20. Sketch of the simplified bifurcation model with the diameter of the parent and daughter airways set as $D = 6\,\text{mm}$. The setup is consistent with the setup employed by Feng and Kleinstreuer, [37]. The gravitational direction is in streamwise direction, i.e. in x_1 direction. The bifurcation angle is set to $\alpha = 60\,°$. Point A denotes the position of the bifurcation carina. The total length of the bifurcation in x_1 is denoted as L_1, while the maximum width in x_2 is denoted as L_2.

of particles with mass inclusions is directly connected to an increased alignment time of the particle with the streamwise direction as the drag component in x_1 is decreased, while the drag component in x_2 is increased. Taken together, the drift away from the (homogeneous) Jeffery orbit towards extended rotational period due to $\hat{m} \uparrow$ significantly affects the particle trajectory. We identified that a particle with mass inclusion has a prolonged alignment time of the long axis with the flow direction and thus exhibit a longer afloat time than the homogeneous counterpart.

5. Bifurcation airway

The final validation case refers to a simplified 3D bifurcating airway as used by Feng and Kleinstreuer, [37], with diameters of the main and secondary airways $D = 6\,\text{mm}$ and a branching angle $\alpha = 60\,°$. The Reynolds number is set to $\text{Re} = 500$, which (according to Zhang et al. [38]) mimics normal breathing conditions in the third generation of an airway. A sketch of the bifurcation model employed is shown in Fig. 20.

In this validation, we analyze the deposition efficiency for different Stokes numbers (Stk) by considering prolate spheroidal particles with an aspect ratio $\lambda = 20$, particle density $\rho_s = 2400\,\text{kg/m}^3$ and an inclusion mass ratio of $\hat{m} = 0$, see Zhang et al. [38].

To compare our results to Zhang et al. [39], Feng and Kleinstreuer, [37], and our previous model for homogeneous particles, see Wedel et al. [30], we assume a uniform inflow velocity and consider 10^4 randomly distributed prolate spheroidal particles with aspect ratio $\lambda = 20$. The fibers are injected with zero initial velocity and angular velocity and with a random orientation at the parent inlet location. Considering a maximum Stokes number of $\text{Stk} = 0.5$, the largest investigated particle volume equivalent diameter is $d_{eq} = 1.8\text{e-}05\,\text{m}$. With an average inlet velocity of $u_{in} = 1.263\,\text{m/s}$, we can approximate the maximum particle Reynolds number as $\text{Re}_{p\,max} = 1.5$. However, note that $\text{Re}_{p\,max}$ only occurs directly at injection time (particles are released with zero initial velocity) as the relative velocity between the fluid and the particle is maximal. Thus, throughout the rest of the simulation $\text{Re}_p \ll \text{Re}_{p\,max}$.

We assume that the particles are deposited as soon as a particle–wall contact is established so that both impaction and interception (particles come close enough to the wall so that a particle edge touches the wall surface) deposition mechanisms are considered. The latter mechanism is particularly crucial for highly elongated particles. In agreement with Zhang et al. [39], it is assumed that non-deposited particles leave the geometry after ten times the average residence time of the flow.

As shown in Fig. 21, we achieve excellent agreement in deposition efficiency between our inhomogeneous particle model with $\hat{m} = 0$ and the reference results (i.e. Feng and Kleinstreuer, [37] as well as our previous model for homogeneous particles, see Wedel et al. [9]). Consequently, we consider the novel inhomogeneous particle deposition model validated for $\hat{m} = 0$ (homogeneous particles).

Next, we investigate the influence of two different inclusion masses, i.e. $\hat{m} = 0.025$ and $\hat{m} = 0.05$. The spherical inclusion is positioned at $\tilde{r}_s = [0.8a_1,\ 0,\ 0]$ and is of size $d_s = 0.15\,d_{eq}$. In this context, the initial position and orientation of the injected particles are randomly generated but identical for all investigated cases ($\hat{m} = 0,\ 0.025, 0.05$). Note that the particle mass is identical for homogeneous and inhomogeneous particles, i.e. m_e is adjusted accordingly. As presented in Fig. 21(b), we observe nearly identical deposition efficiency DE for smaller Stokes numbers $\text{Stk} \leq 1$. However, towards larger Stk the mass inclusion starts to impact the deposition efficiency, where an increase in $\hat{m}$ leads to a decrease in DE.

As observed, modifying the inclusion mass in the spheroidal particle allows for influencing the rotational period leading to a prolonged alignment time of the particle long axis with the flow direction as $\hat{m} \uparrow$. Thus adjusting the mass inclusion of the inhomogeneous particles enables tuning of the overall particle deposition efficiency DE.

Next, we investigate the influence of particle inclusion ($\hat{m} = 0.05$) on particle deposition location for various Stokes number values.

In Fig. 22 the local deposition fraction of the particles is plotted against the streamwise (x_1) and spanwise (x_2) coordinates. As shown in Fig. 22 (a,b), for $\text{Stk} = 0.1$ the particle deposition in x_1 as well as x_2 is slightly influenced by the spherical inclusion, however, the general average deposition location is nearly identical. The particle deposition directly after the bifurcation carina A, see Fig. 22 (a), is slightly reduced for inhomogeneous particles compared to the homogeneous counterpart. This trend intensifies for increasing Stk, see Fig. 22 (b,c) for $\text{Stk} = 0.2$. For $\text{Stk} = 0.5$, the deviations between homogeneous and inhomogeneous particles are strongly pronounced and the average particle deposition of inhomogeneous particles is shifted to the front of the carina.

In general, discrepancies in the deposition fraction of homogeneous and inhomogeneous particles are observed, highlighting the importance of accounting for altered mass distribution. Note that investigating different inhalation regimes (such as cyclic inhalation under resistance) causing a turbulent flow field or deploying a realistic geometry of the respiratory tract are conjectured to lead to even higher discrepancies, which is one of the scopes of our future work.

Taken together, employing inhomogeneous particles offers further tuning parameter to control the motion and deposition of particulate systems. Thus, inhomogeneous particles can offer potential especially in the field of targeted drug delivery, as increased control over particle motion and deposition can lead to an increased efficiency (and thus decrease the side-effects) of the transported drug. Taken together, we observe that modeling realistic particles requires the consideration of mass distribution as non-homogeneous mass distribution can significantly impact the particle translational and orientational dynamics.

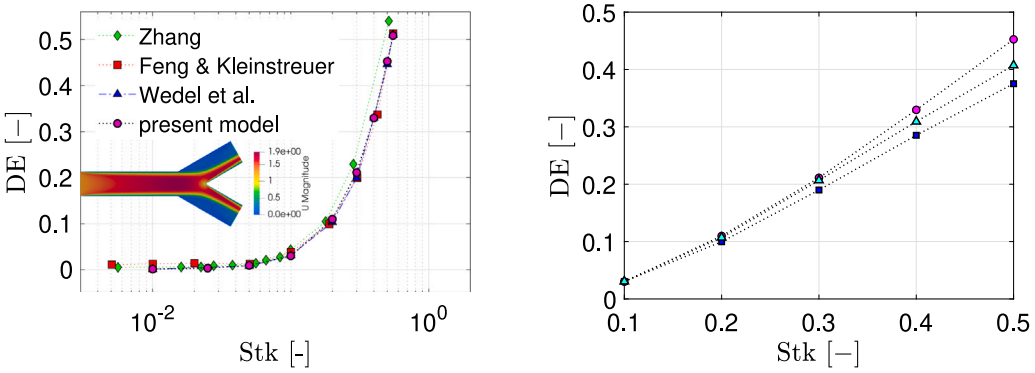

Fig. 21. Deposition efficiency DE [−] in a simplified bifurcation for prolate ellipsoid with $\lambda = 20$. DE denotes the ratio of deposited particles to injected particles. ◆Zhang et al. [39], ■ Feng and Kleinstreuer, [37], ▲ Wedel et al. [9], ● present model. Inclusions $\hat{m}$: ● 0, △ 0.025, ■ 0.05.

6. Conclusion

In this work we investigate kinematics and dynamics of inhomogeneous ellipsoidal particles suspended in viscous fluid. A spherical inclusion models the inhomogeneity in a prolate spheroidal matrix. This approach serves as an extension to the simplified model proposed by Cui et al. [22], in which the coupling of rotational and translational dynamics was neglected in the geometric center formulation. The model is developed in both geometric and a barycenter formulation and both versions are validated by various test cases. First, the inhomogeneous particle settling in vacuum is investigated resulting in excellent agreement between the two formulations. Second, we investigate the settling behavior in stagnant air, where we also observe excellent agreement between the barycenter and the geometric center formulation. Thirdly, we investigate inhomogeneous particles in laminar pipe flow, where identical results to the literature reference were obtained in the limiting case of equal density between ellipsoid and inclusion. We found that a spherical inclusion significantly changes the orientation dynamics of the particles, with the effect being strongly dependent on the size of the inclusion as well as the offset between the barycenter and the geometric center. Finally, we investigated the deposition of ellipsoids with spherical inclusions in a simplified 3D airway bifurcation. We found that inclusions can influence the deposition efficiency and the local particle deposition location, especially for larger Stokes numbers $\mathrm{Stk} > 0.1$. In this context, we observed that an increase in inclusion mass ratio $\hat{m}$ leads to a decrease in the deposition efficiency. In future work, we aim to apply the novel inhomogeneous ellipsoid model to more complex flows, such as flows within a realistic human lung replica as well as gyrotactic swimmers suspended in turbulent flows. In this context, the model enables the study of inhalation and deposition of imperfect glass fiber particles.

CRediT authorship contribution statement

Jana Wedel: Writing – review & editing, Writing – original draft, Visualization, Validation, Software, Methodology, Investigation, Formal analysis, Data curation, Conceptualization. **Paul Steinmann:** Writing – review & editing, Supervision, Resources, Project administration, Methodology, Funding acquisition, Formal analysis. **František Prinz:** Writing – original draft, Visualization, Investigation, Formal analysis. **František Lízal:** Writing – review & editing, Supervision, Project administration, Formal analysis. **Matjaž Hriberšek:** Writing – review & editing, Supervision, Resources, Project administration, Formal analysis. **Jure Ravnik:** Supervision, Resources, Project administration, Formal analysis, Writing – review & editing.

Declaration of competing interest

The authors declare that they have no known competing financial interests or personal relationships that could have appeared to influence the work reported in this paper.

Acknowledgments

The authors thank the Deutsche Forschungsgemeinschaft, Germany for the financial support in the framework of the project STE 544/75-1, the Slovenian Research and Innovation Agency, Germany (research core funding No. P2-0196), and the Czech Science Foundation, Germany project GA22-20357S.

Appendix. Tensor coefficients for prolate spheroidal ellipsoids

In this work, without loss of generality, we focus on the study of prolate spheroidal ellipsoids. For these particles, the tensor coefficients of $\boldsymbol{K}$, $\boldsymbol{\Pi}$ and $\boldsymbol{\Omega}$ can be determined analytically and are functions of the particle aspect ratio ($\lambda = \lambda_1$). The coefficients of the $\boldsymbol{K}$ tensor read in the pFoR as

$$K'_{22} = K'_{33} = \frac{16\left[\lambda^2-1\right]^{3/2}}{\left[2\lambda^2-3\right]\ln(\lambda+\sqrt{\lambda^2-1})+\lambda\sqrt{\lambda^2-1}}, \tag{A.1}$$

$$K'_{11} = \frac{8\left[\lambda^2-1\right]^{3/2}}{\left[2\lambda^2-1\right]\ln(\lambda+\sqrt{\lambda^2-1})-\lambda\sqrt{\lambda^2-1}}. \tag{A.2}$$

To relate $\underline{K'}$ to $\underline{K}$, the resistance coefficient matrix in the iFoR, the rotation matrix $\underline{R}$ is used as

$$\underline{K} = \underline{R}^t\,\underline{K'}\,\underline{R}. \tag{A.3}$$

The tensor coefficients of $\boldsymbol{\Pi}$ and $\boldsymbol{\Omega}$ read in the pFoR as

$$\underline{\Pi'} = \frac{16\,\lambda}{3}\begin{bmatrix} 0 & 0 & 0 \\ 0 & \left[1-\lambda^2\right]\left[ß_2+\lambda^2 ß_3\right]^{-1} & 0 \\ 0 & 0 & -\left[1-\lambda^2\right]\left[ß_1+\lambda^2 ß_3\right]^{-1} \end{bmatrix}, \tag{A.4}$$

$$\underline{\Omega'} = \frac{16\,\lambda}{3}\begin{bmatrix} 2\left[ß_1+ß_2\right]^{-1} & 0 & 0 \\ 0 & \left[ß_2+\lambda^2\,ß_3\right]^{-1}\left[1+\lambda^2\right] & 0 \\ 0 & 0 & \left[ß_1+\lambda^2\,ß_3\right]^{-1}\left[1+\lambda^2\right] \end{bmatrix}, \tag{A.5}$$

by using the non-dimensional coefficients $ß_1$, $ß_2$ and $ß_3$ defined by Gallily and Cohen, [40], as

$$ß_1 = ß_2 = \frac{\lambda^2}{\lambda^2-1} + \frac{\lambda}{2[\lambda^2-1]^{3/2}}\ln\left[\frac{\lambda-\sqrt{\lambda^2-1}}{\lambda+\sqrt{\lambda^2-1}}\right], \tag{A.6}$$

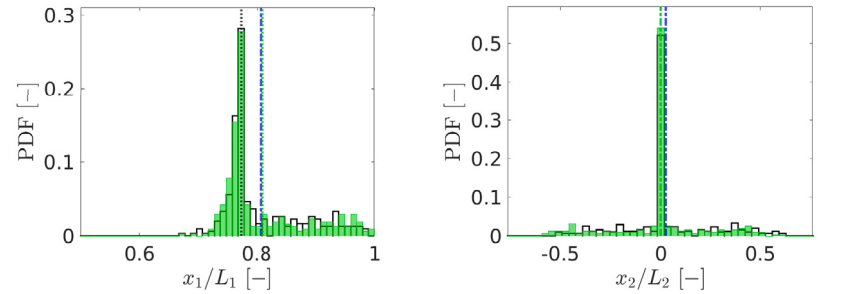

(a) PDF in x_1 direction (Stk = 0.1) (b) PDF in x_2 direction (Stk = 0.1)

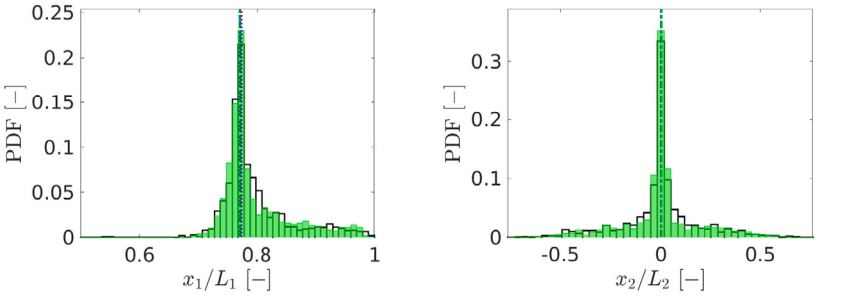

(c) PDF in x_1 direction (Stk = 0.2) (d) PDF in x_2 direction (Stk = 0.2)

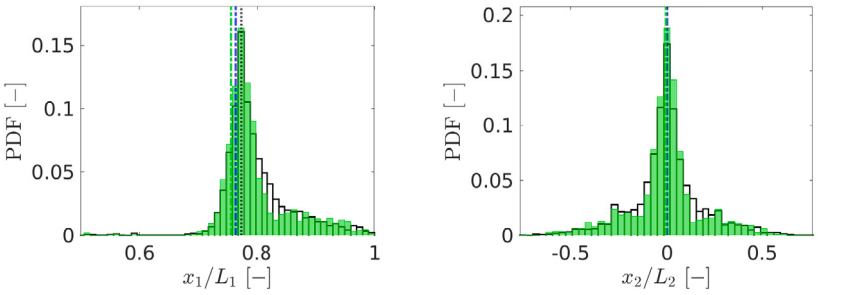

(e) PDF in x_1 direction (Stk = 0.4) (f) PDF in x_2 direction (Stk = 0.4)

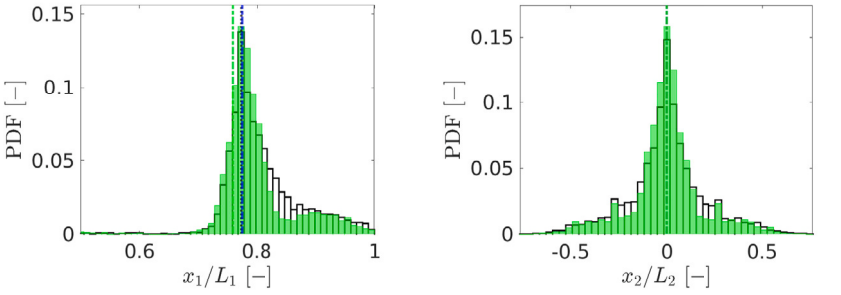

(g) PDF in x_1 direction (Stk = 0.5) (h) PDF in x_2 direction (Stk = 0.5)

Fig. 22. Comparison of particle deposition distribution of homogeneous ($\hat{m} = 0$) and inhomogeneous ($\hat{m} = 0.05$) prolate spheroidal particles with aspect ratio $\lambda = 20$ in a simple bifurcation geometry. Recall that L_1 denotes the maximum length of the bifurcation in x_1 direction (streamwise direction), while L_2 denotes the maximum width in x_2 direction, see Fig. 20. Reference lines: ▪▪▪ location of point A, see Fig. 20. Mean particle positions: ▪▪ homogeneous particle, ▪▪ inhomogeneous particle.

$$ß_3 = -\frac{2}{\lambda^2 - 1} - \frac{\lambda}{[\lambda^2 - 1]^{3/2}} \ln\left[\frac{\lambda - \sqrt{\lambda^2 - 1}}{\lambda + \sqrt{\lambda^2 - 1}}\right]. \tag{A.7}$$

Data availability

Data will be made available on request.

References

[1] Y. Cui, J. Ravnik, P. Steinmann, M. Hriberšek, Settling characteristics of nonspherical porous sludge flocs with nonhomogeneous mass distribution, Water Res. 185 (2019) 159–170.

[2] J. Wedel, M. Štrakl, P. Steinmann, M. Hriberšek, J. Ravnik, Can CFD establish a connection to a milder COVID-19 disease in younger people? Comput. Mech. 67 (2021) 1497–1513, http://dx.doi.org/10.1007/s00466-021-01988-5.

[3] J. Wedel, P. Steinmann, M. Štrakl, M. Hriberšek, J. Ravnik, Risk assessment of infection by airborne droplets and aerosols at different levels of cardiovascular activity, Arch. Comput. Methods Eng. 28 (6) (2021) 4297–4316, http://dx.doi.org/10.1007/s11831-021-09613-7.

[4] J. Wedel, P. Steinmann, M. Štrakl, M. Hriberšek, Y. Cui, J. Ravnik, Anatomy matters: The role of the subject-specific respiratory tract on aerosol deposition—A CFD study, Comput. Methods Appl. Mech. Engrg. (2022).

[5] J. Pallares, A. Fabregat, A. Lavrinenko, H.A. bin Norshamsudin, G. Janiga, D.F. Fletcher, K. Inthavong, M. Zasimova, V. Ris, N. Ivanov, R. Castilla, P.J. Gamez-Montero, G. Raush, H. Calmet, D. Mira, J. Wedel, M. Štrakl, J. Ravnik, D. Fontes, F.J. de Souza, C. Marchioli, S. Cito, Numerical simulations of the flow and aerosol dispersion in a violent expiratory event: Outcomes of the 2022 International Computational Fluid Dynamics Challenge on violent expiratory events, Phys. Fluids 35 (4) (2023) 045106, http://dx.doi.org/10.1063/5.0143795.

[6] P. Koullapis, S.C. Kassinos, J. Muela, C. Perez-Segarra, J. Rigola, O. Lehmkuhl, Y. Cui, M. Sommerfeld, J. Elcner, M. Jicha, I. Saveljic, N. Filipovic, F. Lízal, L. Nicolaou, Regional aerosol deposition in the human airways : The SimInhale benchmark case and a critical assessment of in silico methods, Eur. J. Pharm. Sci. 113 (2017) 1–18, http://dx.doi.org/10.1016/j.ejps.2017.09.003.

[7] P.G. Koullapis, S.C. Kassinos, M.P. Bivolarova, A.K. Melikov, Particle deposition in a realistic geometry of the human conducting airways: Effects of inlet velocity profile, inhalation flowrate and electrostatic charge, J. Biomech. 49 (11) (2016) 2201–2212, http://dx.doi.org/10.1016/j.jbiomech.2015.11.029.

[8] N. Khoa, N. Lu Phuong, K. Takahashi, K. Ito, Transport and deposition of inhaled man-made vitreous and asbestos fibers in realistic human respiratory tract models: An in silico study, Japan Archit. Rev. 5 (2022) http://dx.doi.org/10.1002/2475-8876.12277.

[9] J. Wedel, P. Steinmann, M. Štrakl, M. Hriberšek, J. Ravnik, Shape matters: Lagrangian tracking of complex nonspherical microparticles in superellipsoidal approximation, Int. J. Multiph. Flow 158 (2023) 104283, http://dx.doi.org/10.1016/j.ijmultiphaseflow.2022.104283.

[10] G. Jeffery, The motion of ellipsoidal particles immersed in a viscous fluid, Proc. R. Soc. Lond. Ser. A 102 (715) (1922) 161–179, http://dx.doi.org/10.1098/rspa.1922.0078, URL https://royalsocietypublishing.org/.

[11] H. Brenner, The Stokes resistance of an arbitrary particle, Chem. Eng. Sci. 18 (1) (1963) 1–25.

[12] H. Brenner, The Stokes resistance of an arbitrary particle-IV Arbitrary fields of flow, Chem. Eng. Sci. 19 (10) (1964) 703–727, http://dx.doi.org/10.1016/0009-2509(64)85084-3.

[13] D.O. Njobuenwu, Fairweather M., Dynamics of single, non-spherical ellipsoidal particles in a turbulent channel flow, Chem. Eng. Sci. 123 (2015) 265–282.

[14] S.M.A. Karnis, H.L. Goldsmith, Axial migration of particles in poiseuille flow, Nature 200 (1963) 159–160.

[15] S.M.A. Karnis, H.L. Goldsmith, The flow of suspensions through tubes: V. Inertial effects, Can. J. Chem. Eng. 44 (1966) 181–193.

[16] H. Zhang, G. Ahmadi, F.G. Fan, J.B. McLaughlin, Ellipsoidal particles transport and deposition in turbulent channel flows, Int. J. Multiph. Flow 27 (2001) 971–1009.

[17] P. Mortensen, H. Andersson, J. Gillissen, B. Boersma, Dynamics of prolate ellipsoidal particles in a turbulent channel flow, Phys. Fluids 20 (2008) 093302–093314.

[18] C. Marchioli, M. Fantoni, A. Soldati, Orientation, distribution, and deposition of elongated, inertial fibers in turbulent channel flow, Phys. Fluids 22 (3) (2010) 033301, http://dx.doi.org/10.1063/1.3328874.

[19] L. Tian, G. Ahmadi, Z. Wang, P.K. Hopke, Transport and deposition of ellipsoidal fibers in low Reynolds number flows, J. Aerosol Sci. 45 (2012) 1–18, http://dx.doi.org/10.1016/j.jaerosci.2011.09.001, URL https://www.sciencedirect.com/science/article/pii/S0021850211001571.

[20] Z. Cui, W.-X. Huang, C.-X. Xu, H.I. Andersson, L. Zhao, Alignment of slender fibers and thin disks induced by coherent structures of wall turbulence, Int. J. Multiph. Flow 145 (2021) 103837, http://dx.doi.org/10.1016/j.ijmultiphaseflow.2021.103837, URL https://www.sciencedirect.com/science/article/pii/S0301932221002640.

[21] J. Ravnik, M. Štrakl, J. Wedel, P. Steinmann, M. Hriberšek, Stokes flow induced drag and torque on asbestos-like fibres can not be estimated by a simplistic ellipsoidal approximation, in: 45th International Conference on Boundary Elements and other Mesh Reduction Methods organized by WIT - Wessex Institute of Technology, U.K., 2022.

[22] Y. Cui, J. Ravnik, P. Steinmann, M. Hriberšek, Settling characteristics of nonspherical porous sludge flocs with nonhomogeneous mass distribution, Water Res. 158 (2019) 159–170, http://dx.doi.org/10.1016/j.watres.2019.04.017, URL https://www.sciencedirect.com/science/article/pii/S0043135419303252.

[23] C. Marchioli, H. Bhatia, G. Sardina, L. Brandt, A. Soldati, Role of large-scale advection and small-scale turbulence on vertical migration of gyrotactic swimmers, Phys. Rev. Fluids 4 (2019) 124304, http://dx.doi.org/10.1103/PhysRevFluids.4.124304, URL https://link.aps.org/doi/10.1103/PhysRevFluids.4.124304.

[24] J. Qiu, C. Marchioli, L. Zhao, A review on gyrotactic swimmers in turbulent flows, Acta Mech. Sin. 38 (8) (2022) 722323, http://dx.doi.org/10.1007/s10409-022-22323-x.

[25] R. Rautenbach, S. Hofmann, L. Buntkiel, J. Schäfer, S.F. Reinecke, M. Hoffmann, U. Hampel, M. Schlüter, Dynamics of Lagrangian sensor particles: The effect of non-homogeneous mass distribution, Processes 12 (8) (2024) http://dx.doi.org/10.3390/pr12081617, URL https://www.mdpi.com/2227-9717/12/8/1617.

[26] K.T. Shanley, G. Ahmadi, P.K. Hopke, Y. sung Cheng, Simulated airflow and rigid fiber behavior in a realistic nasal airway model, Particul. Sci. Technol. 36 (2018) 131–140, URL https://api.semanticscholar.org/CorpusID:100488199.

[27] L. Shachar-Berman, S. Bhardwaj, Y. Ostrovski, P. Das, P. Koullapis, S. Kassinos, J. Sznitman, In silico optimization of fiber-shaped aerosols in inhalation therapy for augmented targeting and deposition across the respiratory tract, Pharmaceutics 12 (2020) 230, http://dx.doi.org/10.3390/pharmaceutics12030230.

[28] C. Wang, K.-W. Yan, Y.-D. Lin, P. Hsieh, Biodegradable core/shell fibers by coaxial electrospinning: Processing, fiber characterization, and its application in sustained drug release, Macromolecules 43 (2010) http://dx.doi.org/10.1021/ma100423x.

[29] F. Lízal, M. Cabalka, M. Maly, J. Elcner, M. Belka, E.L. Sujanska, A. Farkas, P. Starha, O. Pech, O. Misik, J. Jedelsky, M. Jicha, On the behavior of inhaled fibers in a replica of the first airway bifurcation under steady flow conditions, Aerosol Sci. Technol. 56 (4) (2022) 367–381, http://dx.doi.org/10.1080/02786826.2022.2027334.

[30] J. Wedel, M. Štrakl, P. Steinmann, M. Hriberšek, J. Ravnik, A novel particle–particle and particle–wall collision model for superellipsoidal particles, Comput. Part. Mech. (2023) http://dx.doi.org/10.1007/s40571-023-00618-6.

[31] H. Goldstein, Classical Mechanics, second ed., Reading, MA, Addison-Wesley, 1980.

[32] H. Lamb, Handbook of Fluid Dynamics, sixth ed., Cambridge University Press, 1994.

[33] D. Di Giusto, L. Bergougnoux, C. Marchioli, l. Guazzelli, Influence of small inertia on Jeffery orbits, J. Fluid Mech. 979 (2024) A42, http://dx.doi.org/10.1017/jfm.2023.1007.

[34] Y. Cui, J. Ravnik, O. Verhnjak, M. Hriberšek, P. Steinmann, A novel model for the lift force acting on a prolate spheroidal particle in an arbitrary non-uniform flow. Part II. Lift force taking into account the non-streamwise flow shear, Int. J. Multiph. Flow 111 (2019) 232–240.

[35] Y. Cui, J. Ravnik, M. Hriberšek, P. Steinmann, A novel model for the lift force acting on a prolate spheroidal particle in an arbitrary non-uniform flow. Part I. Lift force due to the streamwise flow shear, Int. J. Multiph. Flow 104 (2018) 103–112.

[36] Y. Cui, J. Ravnik, M. Hriberšek, P. Steinmann, On constitutive models for the momentum transfer to particles in fluid-dominated two-phase flows, Adv. Struct. Mater. 80 (2018) 1–25.

[37] Y. Feng, C. Kleinstreuer, Analysis of non-spherical particle transport in complex internal shear flows, Phys. Fluids 25 (2013) 1904, http://dx.doi.org/10.1063/1.4821812.

[38] L. Zhang, B. Asgharian, S. Anjilvel, Inertial and interceptional deposition of fibers in a bifurcating airway, J. Aerosol Med. 9 (3) (1996) 419–430.

[39] H. Zhang, D. Li, L. Xie, Xiao Y., Documentary research of human respiratory droplet characteristics, in: P. Engineering (Ed.), 9th International Symposium on Heating, Ventilation and Air Conditioning (ISHVAC) and the 3rd International Conference on Building Energy and Environment, COBEE, vol. 121, 2015, pp. 1365–1374.

[40] I. Gallily, A.-H. Cohen, On the orderly nature of the motion of nonspherical aerosol particles II. Inertial collision between a spherical large droplet and axially symmetrical elongated particle, J. Colloid Interface Sci. 68 (1979) 338–356.